HIGH TEMPERATURE OXIDATION KINETICS OF A Zr-2½ w/o Nb ALLOY

by

VINCENT F. URBANIC, B.Sc. (Met.)

A Thesis

Submitted to the Faculty of Graduate Studies

in Partial Fulfillment of the Requirements

for the Degree

Master of Science

McMaster University

April, 1970.

MASTER OF SCIENCE (1970)
(Metallurgy)

McMASTER UNIVERSITY
Hamilton, Ontario

TITLE: High Temperature Oxidation Kinetics of a Zr-2½ w/o Nb Alloy

AUTHOR: Vincent F. Urbanic, B.Sc. (Met.), McMaster University
Hamilton, Ontario

SUPERVISOR: Dr. W. W. Smeltzer

NUMBER OF PAGES: (viii) and 102

SCOPE AND CONTENTS:

An investigation is reported on the oxidation kinetics of a Zr-2½ w/o Nb alloy in the temperature range 650° - 1000°C in pure oxygen atmospheres. Weight gain data is presented for rectangular plate specimens in the range 650° - 991°C. The kinetics were determined continuously using thermogravimetric techniques and may be represented by a parabolic relationship followed by essentially linear kinetics over the range 650° - 885°C, while over the range 937° - 991°C, parabolic kinetics is followed by a breakaway transition to an increasing reaction rate. In the low temperature range the parabolic rate constant has been calculated to be $k_p = 20.8 \exp\left(-\frac{38026}{RT}\right)$ and in the high temperature range $k_p = 0.22 \exp\left(-\frac{30054}{RT}\right)$.

The latter part of the investigation was focused on the oxidation of Zr-2½ w/o Nb at 1000°C in pure oxygen for periods extending to 23 hours. The morphological development of the oxide scale and metal substrate during parabolic oxidation was investigated and is supported by kinetic, X-ray, electron micro-probe and metallographic observations. Spherical specimens

were used to minimize edge effects and hence extend the period of parabolic behaviour. The observed microstructures are discussed with reference to the Zr-Nb-O phase diagram.

A qualitative discussion pertaining to observations related to the breakaway phenomenon is also presented.

ACKNOWLEDGMENTS

The author wishes to express his gratitude to his supervisor, Dr. W. W. Smeltzer for his guidance and contribution throughout the investigation; to R. Foster for his practical advice and assistance with the experimental apparatus; to the Atomic Energy of Canada Ltd., Chalk River, for kindly supplying the alloy.

TABLE OF CONTENTS

		Page
CHAPTER I	Introduction	1
CHAPTER II	Review of Literature	3
2.1	Introduction	3
2.2	Oxidation of Metals	3
2.2.1	Structure of Oxides	3
2.2.2	Oxidation Rates	5
2.2.3	Oxidation Rate as a Function of Temperature	8
2.2.4	Oxidation Rate as a Function of Pressure	9
2.2.5	Mechanisms of Scale Formation	10
2.3	Oxidation of Alloys	14
2.3.1	Wagner-Hauffe Model	14
2.3.2	Selective Oxidation	15
2.3.3	The Formation of Composite Scales	16
2.3.4	The Formation of Scales with Complex Oxides	17
2.3.5	Internal Oxidation	17
CHAPTER III	Oxidation of Zirconium, Niobium and Zirconium-Niobium Alloys	19
3.1	Oxidation of Zirconium	19
3.2	Oxidation of Niobium	23
3.3	Oxidation of Zr-Nb Alloys	24
CHAPTER IV	Experimental	28
4.1	Introduction	28
4.2	Apparatus	28
4.3	Procedure	32
4.4	Materials and Preparations	34
CHAPTER V	Results and Observations	38
5.1	Introduction	38
5.2	Zr-2½ w/o Nb Alloy Prior to Oxidation	40
5.3	Oxidation Measurements at 991°C and 937°C	40
5.4	Oxidation Measurements from 885°C to 650°C	46
5.5	X-Ray Measurements	57
5.6	Oxidation Measurements at 1000°C	58
5.7	Metallography and Microscopic Observations	62
5.8	Electron Micro-probe Results	72

Table of Contents (contd.)

CHAPTER VI	Discussion	75
6.1	Oxidation Rate as a Function of Temperature	75
6.2	X-Ray Analyses	79
6.3	Oxidation of a Zr-2½ w/o Nb Alloy at 1000°C	80
6.4	Breakaway Oxidation	88
CHAPTER VII	Conclusions	92
APPENDIX		95
LIST OF REFERENCES		100

LIST OF ILLUSTRATIONS AND TABLES

		Page
Figure 1	Zr-O and Nb-O Phase Diagrams	20
Figure 2	Zr-Nb-O Ternary Phase Diagram (1500°C isotherm)	25
Figure 3	Schematic Diagram of the Apparatus	29
Figure 4	Schematic Diagram of the Polishing Jig	35
Figure 5	Zr-Nb Phase Diagram	39
Figure 6	Microstructure of the Alloy Prior to Oxidation	41
Figure 7	Oxidation Rate of Zr-2½ w/o Nb at 991°C	42
Figure 8	Oxidation Rate of Zr-2½ w/o Nb at 937°C	43
Figure 9	Oxidation Rate of Zr-2½ w/o Nb at 991°C (parabolic plot)	44
Figure 10	Oxidation Rate of Zr-2½ w/o Nb at 937°C (parabolic plot)	45
Figure 11	Topography of Sample Oxidized at 991°C	47
Figure 12	Oxidation Rate of Zr-2½ w/o Nb at 885°C	48
Figure 13	Oxidation Rate of Zr-2½ w/o Nb at 832°C, 800°C and 750°C	49
Figure 14	Oxidation Rate of Zr-2½ w/o Nb at 700°C and 650°C	50
Figure 15	Oxidation Rate of Zr-2½ w/o Nb at 885°C (parabolic plot)	52
Figure 16	Oxidation Rate of Zr-2½ w/o Nb at 832°C, 800°C and 750°C (parabolic plot)	53
Figure 17	Oxidation Rate of Zr-2½ w/o Nb at 700°C and 650°C (parabolic plot)	54
Figure 18(a)	Micrographs of Oxidized Plate Samples	55
Figure 18(b)	Topography of Sample Oxidized at 885°C	56
Figure 18(c)	Micrograph of Spherical Samples Oxidized at 1000°C	59

Page

Figure 19 Oxidation Rate of Zr-2½ w/o Nb at 1000°C 60

Figure 20 Oxidation Rate of Zr-2½ w/o Nb at 1000°C (parabolic plot) 61

Figures 21-23 Cross Sections of Zr-2½ w/o Nb Oxidized at 1000°C 63-65

Figure 24 "Top View" of the Columnar Precipitate Region 67

Figure 25 Micrograph Showing the Fine Columnar Regions and Differing Intercolumnar Constituents 68

Figure 26 Cross Sections of the Internal Oxidation Zone 69

Figure 27 Plot of the Thickness of the α + Oxide Zone versus Time 70

Figure 28 Plot of the Thickness of the α + β Zone versus Time 71

Figure 29 Cross Section of the Multiphase Oxide Scale Near the Alloy/Oxide Interface 73

Figure 30 Arrhenius Plot of Log k_p versus $\frac{1}{T}$ (°K) 77

Figure 31 Schematic Representation of the Cross Section and the Composition Path Defining the Observed Structures 82

Figure 32 Cross Section Showing Secondary Nucleation of α-plates in the α + β Precipitate Region 86

Figure 33 Cross Sections Showing Initiation of Localized Attack and a Region of Localized Attack (Breakaway) 90

TABLES

I Parabolic Oxidation Rate Constants 95

II X-Ray Diffractometer Data for Bulk Oxide Formed at 991°C 96

III X-Ray Diffractometer Data for Oxide at the Alloy/Oxide Interface 97

IV Oxygen Distribution at Various Temperatures 98

CHAPTER I

Introduction

In the rapidly advancing field of nuclear technology, zirconium and its alloys have assumed a significant role. The development of zirconium-base alloys is being forced by the demands for stronger and lighter sections of more corrosion-resistant materials having low neutron absorption cross section for structural use, such as pressure tubes, in nuclear reactor systems. In the development work on zirconium-base alloys for application in water reactors, alloys containing niobium are receiving increasing attention with respect to having the best combination of strength, ductility, corrosion resistance and neutron economy.

In this investigation, the behaviour of a Zr-2½ w/o Nb alloy oxidized in a pure oxygen atmosphere in the temperature range 650° - 1000°C is reported. The study may be divided into two parts: the first part consists of kinetic data compiled over the entire temperature range using rectangular plate samples while the second part is focused on the morphological development of the oxide scale and metal substrate at 1000°C and is supported by kinetic, X-ray, electron micro-probe and metallographic observations.

A brief outline of the fundamental principles and theories pertaining to high temperature oxidation is given as well as a review of other investigations of zirconium, niobium and zirconium-niobium alloy oxidation. This is followed by some experimental results from the author's investigation and an attempt has been made to explain the results on the basis of

these theories and principles. Direct comparison of results with other investigators is difficult due to differences in experimental conditions; however, any agreements or disagreements between experimental observations are qualitatively discussed.

CHAPTER II

Review of Literature

2.1 Introduction

Metal oxidation pertains to the reaction of a metal with oxygen to produce a reaction product consisting of one or more oxides. This reaction is of a more complex nature than it appears. It was not long ago that mechanisms of metal oxidation were based on the simple concepts for diffusion of metal or non-metal ions through the oxide lattice. However, investigators during the past two decades have shown that other factors such as the structures of the metal and oxide, mechanical properties of the oxide, nucleation, oxide compositions and oxygen solution in the metal, etc., may influence the process of metal and alloy oxidation. Consequently simple metal or oxygen ion diffusion through the oxide lattice only determines the rate of oxidation in a few idealized cases.

It is the purpose of this chapter to briefly summarize the principles of metal and alloy oxidation. A more thorough description of the topic may be found in many standard texts[1,2,3].

2.2 Oxidation of Metals

2.2.1 Structure of Oxides

An understanding of the nature of oxides is necessary before discussing oxidation mechanisms. Practically all oxides are semiconductors,

and electrical conduction may occur either by positive holes (p-type semiconduction) or by electrons (n-type semiconduction). Wagner proposed that oxide semiconductors are not of exact stoichiometric composition, but may contain an excess of cations or anions. Consequently, oxides may have cation or anion vacancies or ions in interstitial positions in the lattice.

A metal deficit (p-type) oxide is one having vacant cation sites and electrical neutrality is maintained by the formation of higher valence cations or positive holes. The model for a metal excess (n-type) oxide is one in which there are metal ions in interstitial positions or anion vacancies in the lattice and free electrons. The validity of these models has been demonstrated by means of electrical conductivity measurements on the oxide. The defect equations generated from the models relate the concentration of the defects to the oxygen pressure. Since the conductivity is proportional to the defect concentration, its dependence on the oxygen pressure may be experimentally verified.

The fact that an oxide may exhibit a variable composition range is important when considering metal oxidation reactions. The nature of the defect structure of the oxide which occurs in a particular case partially determines the oxidation rate. For an oxide layer growing on a metal, an oxygen pressure gradient and a defect gradient exists across the oxide. A concentration gradient across a single solid phase causes diffusion of ions via interstitial or vacant lattice sites. Thus a knowledge of the defect structure and the nature of the diffusing species is necessary in order to understand the oxidation mechanism.

2.2.2 Oxidation Rates

Reaction rates and corresponding rate equations for the oxidation of a metal are functions of a number of factors such as temperature, oxygen pressure, surface preparation and pretreatment of the metal. Although interpretations of oxidation mechanisms cannot be made from rate equations alone, these equations can be used to classify the oxidation behaviour of metals and thus limit the interpretation to a certain group of mechanisms. The number of possible mechanisms may be reduced or the proper one may be deduced by correlation with other studies. Kinetic data obtained from metal-gas studies are most often compiled in the form of weight gain per unit area, $\frac{\Delta m}{A}$, as a function of time, t. In many cases, the increase in weight can be related to the thickness of the oxide film if the density and molecular volume of the oxide are known.

The rate equations which are most commonly encountered may be described as logarithmic, parabolic or linear; these represent only limiting and ideal cases and deviations from these rate equations may occur.

Logarithmic rate equations,

$$\text{Direct logarithmic:} \quad \left(\frac{\Delta m}{A}\right) = K_{log} \cdot \log(a.t + to) \qquad (2\text{-}1)$$

$$\text{Inverse logarithmic:} \quad \frac{1}{\left(\frac{\Delta m}{A}\right)} = B - K_{il} \cdot \log t \qquad (2\text{-}2)$$

are characteristic of the oxidation of a large number of metals at low temperatures (below 300^{o}- 400^{o}C) where the thin film range exists (about 100 Å). $\frac{\Delta m}{A}$ is the weight grain per unit area, t is the time and K_{log} and K_{il} are the rate constants; a, B and to are constants. The model for the thin film range is based on the hypothesis, originally proposed by Mott[4], that a strong electric field exists across the oxide film, and this field is

responsible for pulling anions or cations through the oxide phase. The electrical charge distribution arises from electrons passing from the metal to the gas/oxide interface. The passage of metal or oxygen ions into the oxide then determines the reaction rate. Thus at low temperatures and for very thin film thicknesses, the ions do not simply diffuse through the film under the influence of a concentration gradient.

The parabolic rate law was first formulated by Tammann[5] and, in an independent investigation by Pilling and Bedworth[6]. The rate of oxidation is inversely proportional to the film thickness:

$$\frac{dx}{dt} = \frac{k'_p}{x} \tag{2-3}$$

or, on integration:

$$x^2 = k_p t + c \tag{2-4}$$

In terms of weight gain,

$$\left(\frac{\Delta m}{A}\right)^2 = K_p t + c_p \tag{2-5}$$

where K_p is the parabolic rate constant, and c_p is a constant of integration. The parabolic relationship can be derived from Wagner's theory of oxidation[7,8]. As a rule, high temperature parabolic oxidation indicates that a diffusion process is rate determining. Such a process may include a uniform diffusion of one or both of the reactants through a growing compact scale or a uniform diffusion of gas into the metal.

In some cases, kinetic data for metals exposed to oxygen have been found to follow a cubic rate law, which is intermediate between the logarithmic and the parabolic relations:

$$\left(\frac{\Delta m}{A}\right)^3 = K_c t \qquad (2\text{-}6)$$

This relationship can be theoretically derived and explained by the Mott-Cabrera mechanism[4] for metal deficit oxide films but fails to explain the cubic oxidation of metals forming n-type oxides such as titanium and zirconium. However, the same data can be approximated by other rate laws.

The simplest rate expression is the linear equation, where the thickness of the film has no influence on the rate of uptake of oxygen. Linear oxidation may be described by:

$$\frac{dx}{dt} = k_\ell \qquad (2\text{-}7)$$

which on integration gives:

$$x = k_\ell t + c \qquad (2\text{-}8)$$

In terms of weight gains:

$$\left(\frac{\Delta m}{A}\right) = K_L t + c_L \qquad (2\text{-}9)$$

where K_L is the linear rate constant and c_L is the integration constant. A linear relationship signifies that the surface or phase boundary reaction is the rate determining step. If the oxide is non-protective with no barrier between the gas phase and the metal surface, the linear law is expected to hold. Metals which have a tendency to oxidize at a linear rate usually have porous or cracked oxides and generally have a low or high volume ratio of oxide formed to metal consumed, generally known as the Pilling and Bedworth ratio. If this ratio is less than unity, the oxide may

be under tension which could be relieved by the development of cracks. An oxide exhibiting a larger volume than the consumed metal would tend to be of a compact structure and the kinetics would be diffusion controlled. If this ratio is exceptionally high, porous or cracked scales may result due to the effect of high compressive stresses in the oxide. However, it must be pointed out that the Pilling and Bedworth rule is only used as a rough guide since there are exceptions to the rule.

Oxidation reactions are frequently found to follow a combination of rate laws. This may mean that the oxidation reaction occurs by two simultaneous mechanisms, one predominating during the initial stages while the other predominates after extended oxidation, or, that changes may take place in the rate determining mechanism as a result of changes in the nature of the oxide scale. For example, at high temperatures, a combination of parabolic and linear oxidation kinetics may occur giving rise to paralinear oxidation. This may occur as a result of a compact scale growing initially at a parabolic rate, transforming at a linear rate to an outer porous and non-protective oxide layer. Observations of this type of kinetics has been reported by Smeltzer and Akram[9] for the oxidation of zirconium.

2.2.3 Oxidation Rate as a Function of Temperature

Surface reactions, being kinetic processes, may be expected to obey Arrhenius's equation,

$$k = A \cdot \exp^{-Q/RT} \qquad (2\text{-}10)$$

where k is the oxidation rate constant, A is a constant having the same

units as k, Q is the activation energy required for oxidation, R is the gas constant and T is the absolute temperature. The experimentally determined values of k, when plotted on a logarithmic scale against the reciprocal of the absolute temperature often yield a straight line, where slope is simply related to the activation energy by a factor of R^{-1}. The exponential temperature dependence of the oxidation rate is upheld for many systems. There are, however, a few exceptions where the rate is independent of temperature. For example, the oxidation of niobium at high temperatures is not well reproducible[10] and hence no simple Arrhenius relationships can be attained. As a rule, the activation energy remains constant as long as the same rate-determining mechanism prevails, and changes in the temperature dependence may therefore signify changes in the oxidation mechanism[11,12].

2.2.4 Oxidation Rate as a Function of Pressure

In metal oxidation studies, determination of the oxygen pressure dependence may aid in the interpretation of oxidation mechanisms. If adsorption is the rate controlling step, then the reaction exhibits a large oxygen pressure dependence. At low oxygen pressures, the oxidation rates are found to be proportional to $P_{O_2}^{\frac{1}{2}}$ suggesting a dissociative reaction on the surface, with an adsorption equilibrium established on the surface.

$$O_2^{(g)} \rightleftarrows 2O_{ads} \qquad (2\text{-}11)$$

If the reaction is controlled by solid state diffusion, interface reactions are rapid compared to the rates of diffusion. Wagner's theory assumes thermodynamic equilibrium at the gas/oxide and metal/oxide interfaces, and the oxygen pressure dependence is determined by the defect

structure and the dissociation pressure of the oxide. If the dissociation pressure is negligible compared to the ambient oxygen pressure, parabolic oxidation is independent of oxygen pressure for n-type oxides and proportional to $P_{O_2}^{1/n}$ for p-type oxides, where $n \geq 2$ and is a function of the defect structure of the oxide. The independence of oxygen pressure on the oxidation rate for n-type scales has been shown by Hussey and Smeltzer[13] and Gulbransen and Andrew[14] for the reaction of zirconium with oxygen. The number of defects at the oxide/gas interface for ZrO_2 may be expected to be negligibly small at moderate temperatures and pressures, and consequently the oxidation rate should be nearly independent of the partial pressure of oxygen.

2.2.5 Mechanisms of Scale Formation (Parabolic Oxidation)

As oxidation proceeds beyond the point where electron field effects can be neglected, parabolic oxidation is frequently observed. The mechanism for parabolic oxidation has been described by Wagner[7]. The mechanism is controlled by diffusion of reactants along a concentration gradient in a semi-conducting oxide. Wagner derived an expression for the rate of oxide growth in terms of the specific conductivity of the oxide, K, the transport number of the cations, anions and electrons, τ_c, τ_A and τ_e, and the decrease in free energy of the oxidation reactions expressed in terms of the generated electromotive force, E_o, all measurable quantities. Considering the transport of both ions and electrons through the scale, the resistance (both electrolytic and electronic) of the film was derived, which when substituted into a form of Faraday's law gives:

$$\frac{dn}{dt} = \frac{(\tau_c + \tau_A)\,\tau_e K A E_o}{96500\,\xi} \qquad (2\text{-}12)$$

where n is the g-equivalents of oxide, t is time (secs.), A is the area of the film (cm^2) and ξ is the film thickness (cm). (2-12) is the simplest form of the equation derived by Wagner. $\frac{dn}{dt}$ is related to the parabolic rate constant, k_p, for an oxide M_2O, by the following:

$$\frac{dn}{dt} = \tfrac{1}{2} V_{eq} \left(\frac{Z}{M}\right)^2 k_p \qquad (2\text{-}13)$$

where V_{eq} = vol. of 1 g-equivalent of oxide, Z = the valency of oxygen ion and M = atomic weight of oxygen. Theory and experiment can be compared using relations (2-12) and (2-13) respectively. Since K can vary with pressure according to the relation

$$K = K_o P_{O_2}^{1/n} \qquad (2\text{-}14)$$

(2-12) was expanded to include this pressure dependence. The expression is:

$$\frac{dn}{dt} = \frac{(\tau_A + \tau_c)\tau_e K_o A}{96500\,\xi} \cdot \frac{1.983\,nT}{23066\,Z} \left(P_x^{1/n} - P_x^{diss}\right) \qquad (2\text{-}15)$$

where $P_x^{1/n}$ is the gas pressure at the oxide surface, P_x^{diss} is the dissociation pressure of the oxide (at the metal/oxide interface) and T is the absolute temperature.

Calculating the mobilities of ions and electrons and considering that the chemical potential is a linear function of log P_x, Wagner obtained the following equation:

$$\frac{dn}{dt} = \left\{ \frac{300\ A}{96500\ N_e} \int_{\mu_x(m)}^{\mu_x(s)} (\tau_c + \tau_A)\tau_e\ K \frac{1}{Z_x}\ d\mu_x \right\} \frac{1}{\xi} \qquad (2\text{-}16)$$

where N is Avogadro's number, e the electronic charge, $\mu_x(s)$ and $\mu_x(m)$ are the chemical potentials of the anions at the oxide/gas and metal/oxide intefaces respectively, and Z_x is the valancy of the anionic species. The expression in the brackets is called the rational rate constant, k_r, and using the fact that ion mobilities can be expressed in terms of self-diffusion coefficients, an alternate expression for k_r is obtained:

$$k_r = C_i \int_{a_c(s)}^{a_c(m)} (D_c^* + \frac{Z_x}{Z_c} D_x^*)\ d\ln a_c \qquad (2\text{-}17)$$

or

$$k_r = C_i' \int_{a_x(m)}^{a_x(s)} (\frac{Z_c}{Z_x} D_c^* + D_x^*)\ d\ln a_x \qquad (2\text{-}18)$$

where $C_i = Z_c C_c = Z_x C_x$ in the concentration of non-metal or metal ions, a_c and a_x are activities of the metal and non-metal species and D_c^* and D_x^* are the self-diffusion coefficients of the metal and non-metal respectively.

Deviations from true parabolic relationships may occur as a result of short circuit diffusion paths such as grain boundaries and dislocations in the oxide. Smeltzer et al.[15] derived a rate equation taking this effect into account by assuming that the fraction of total sites, f, available for the diffusing species in short circuit paths decayed exponentially with time. Their result

$$x^2 = k_p \left[t + \frac{f^o \alpha}{k} \left\{ 1 - \exp(-kt) \right\} \right] \qquad (2\text{-}19)$$

where x = the film thickness, k_p = the parabolic rate constant, t = the time, $\alpha = \frac{D_B}{D_L}$ and k = a constant agreed well with experimental data for the oxidation kinetics of hafnium, titanium and zirconium.

Deviations from true parabolic behaviour such as paralinear kinetics are also observed. Wagner[16] pointed out that this type of behaviour exists when a scale consists of a compact adherent scale underlying a porous one. The observed kinetics are a result of the inner oxide growing parabolically, transforming to a porous outer oxide at a constant rate and therefore reaches a limiting thickness.

Transition from an initial parabolic or cubic rate to a more rapid kinetics is often termed "breakaway oxidation" and is commonly observed during oxidation of zirconium and its alloys[17,18]. No definite mechanism of the oxidation rate transition is known; however, currently proposed mechanisms have been classified into three groups[19]:

(i) changes in stoichiometry of the oxide due to oxygen saturation induces fracture thus leading to breakaway transition.

(ii) transition attributed to crystallographic changes in the oxide.

(iii) rate transition considered in terms of (a) mechanical failure of the oxide, or (b) a change of the properties of the oxide due to recrystallization of the metal.

2.3 Oxidation of Alloys

The purpose of most studies of alloy oxidation is to improve the oxidation resistance of pure metals. A qualitative treatment on the effect of alloying on oxidation has been given in reviews by Stringer[20] who classifies the effects into seven major categories, and by Bénard[21].

2.3.1 Wagner-Hauffe Model

The Wagner-Hauffe model is simple in principle and can be found in practically all standard texts[1,2,3]. It may be applied to metals which follow the Wagner oxidation mechanism. Since the rate is dependent on the rate of diffusion of defects, the oxidation rate is changed by altering the defect concentration in the scale by addition of foreign atoms. Briefly the rule states that addition of an alloying element which exhibits a valence state higher than that of the base metal will decrease the concentration of defects in an n-type oxide, and hence reduce the oxidation rate. For a p-type oxide, an element of higher valency increases the defect concentration and thus the oxidation rate. For ionically conducting scales, the slow transport of electrical defects is the rate controlling step. Thus for cationic conduction by vacancies or interstitials, a higher valency cation reduces the positive hole concentration or increases the concentration of electrons respectively and hence decreases or increases the rate respectively. For anionic conduction by vacancies or interstitials, a higher valency cation will increase the electron concentration or decrease the concentration of positive holes respectively thus increasing or decreasing the rate respectively. This model is based on the assumption

that the foreign ions are dissolved substitutionally on the parent oxide and usually breaks down when the alloy content exceeds 2 or 3 wt. %.

2.3.2 Selective Oxidation

In selective oxidation, the least noble metal selectively oxidizes and this phenomenon is favoured when the oxides of the alloying components show large differences in stability. If the minor element is oxidized, either a continuous layer of oxide forms at the alloy surface or the oxide remains dispersed in the interior of the metal. The latter is more commonly termed "internal oxidation" and is a result of rapid diffusion of oxygen in the alloy. If oxygen diffusion is relatively slow, the minor element oxidizes to form a continuous layer on the surface.

When only the major element is oxidized, the minor element is dispersed either as small metallic particles in the oxide or as the layer of metal just below the oxide. In the latter case, the enriched region can act as a diffusion barrier and alter the stability of a planar metal/oxide interface[22]. If oxidation is determined by the diffusion of metal through the barrier, oxidation will be most rapid at the thinnest regions making the metal surface more irregular. On the other hand, if the oxidation rate is determined by diffusion through the scale, the interface will tend to remain planar.

The factors determining the oxidation of alloys with a noble alloying element were investigated by Wagner[23] using the nickel-platinum system. With the aid of derived mathematical expressions pertaining to the system where the noble element is practically unaffected by oxygen, the dependence of oxidation rate on the composition of the binary alloy system was discussed.

2.3.3 The Formation of Composite Scales

Unlike the systems previously described where only one element reacts with oxygen, most binary systems A-B are such that both oxides could be formed resulting in the formation of composite scales. A theoretical analysis of the diffusion processes in both the alloy and the oxide phase during the oxidation of alloy phases leading to composite scales has been given by Wagner[23,24]. In considering an alloy A-B in which B is the less noble metal and no double oxides or spinels are formed, three cases are considered. At low concentrations of B in the alloy, N_B', A oxide is formed. As oxidation proceeds, B is enriched at the alloy/oxide interface and the B oxide will begin to form when the concentration of B reaches the equilibrium concentration of B, N_B^*, in the mixture (alloy + A oxide + B oxide). For this mechanism N_B' is smaller than N_B^*. Similarly for high concentrations of B in the alloy, N_B'', only the B oxide will be formed. The formation of A oxide will begin only when the concentration of A at the interface reaches the critical concentration $N_A^* = 1 - N_B^*$ corresponding to the three phase equilibrium. For this mechanism N_B'' is greater than N_B^*. At concentrations ranging from N_B' to N_B'' the A oxide and B oxide will be formed simultaneously. From Wagner the critical concentration, N_B'', above which only the B oxide is formed is given by:

$$N_B'' = \frac{V}{16 Z_B} \left(\frac{\pi k_p}{D} \right)^{\frac{1}{2}} \qquad (2\text{-}20)$$

where V = the molar volume of the alloy, Z_B = the valence of the B atoms, D = the diffusion coefficient of B in the alloy and k_p = the parabolic rate constant for exclusive formation of B oxide. Below this concentration

results in the simultaneous formation of both oxides.

2.3.4 Formation of Scales with Complex Oxides

When the oxides of alloying components react with each other to form a more stable complex oxide, at least part of the oxide scale will consist of the complex oxide. These more stable forms may be double oxides or spinels. Of the double oxides, the silicates are of importance because they may form glass-like layers in which diffusion is slow. In the case of alloy steels, spinels are frequently encountered upon oxidation. The formation of complex oxides have been extensively studied in alloys containing Fe, Ni and Cr. Protective scales on high temperature oxidation-resistant alloys often consists of complex oxides. It has been demonstrated that diffusion rates in double oxides and spinels are often appreciably smaller than in the pure oxides.

2.3.5 Internal Oxidation

When oxygen dissolves in the alloy phase during oxidation, the less noble component may form an oxide within the alloy. This phenomenon has been termed internal oxidation. Internal oxidation requires that the rate of diffusion of oxygen in the alloy be appreciably faster than that of the alloying element. Oxygen diffusing down its gradient can react with the less noble constituent to form its oxide. If the oxygen partial pressure of the oxidizing atmosphere is suficiently low, formation of an outer scale can be avoided. However, at higher oxygen pressures, an outer scale is formed as well as a subscale. There are two possibilities in which this may occur: the same oxide constitutes the scale and the subscale, or the

solute metal provides the oxide for the subscale while the outer scale consists mainly of the oxide of the solvent.

The first situation was discussed by Thomas[25] with respect to the oxidation of alloys of noble metals with Cu. Assuming that the various concentration gradients are linear, that the internal precipitates offer no resistance to diffusion and that the diffusion rate of oxygen and its maximum solubility in the alloy is independent of composition, Fick's laws were applied and expressions describing the rate constants of parabolically growing scales and subscales were derived. There was agreement between the calculated and experimental values. The second situation was discussed by Rhines et al[26] employing similar assumptions.

The various forms of internal oxidation have been classified by Moreau and Bénard[27] while Rapp[28] has considered in detail the kinetics, microstructures and mechanism of internal oxidation in five alloy types.

CHAPTER III

Oxidation of Zirconium, Niobium and Zirconium-Niobium Alloys

3.1 Oxidation of Zirconium

The oxidation of zirconium has undergone extensive investigation over the last twenty years due to the importance of zirconium alloys in nuclear reactor technology. The Zr-O phase diagram is given in Fig. 1(a) and aids in understanding the oxidation procedure. Below 862°C zirconium exists as h.c.p. α-Zr which has a high solubility for oxygen (~30 a/o). Above 862°C pure zirconium exists as β-Zr and exhibits a b.c.c. structure. The solubility of oxygen in β-Zr is much smaller and as a result, saturation of the β phase with oxygen leads to the stabilization of α-Zr.

In general, oxidation studies of α-Zr in oxygen have yielded data that corresponds to a cubic rate law[29-32] or a parabolic rate law[13,32-34] or rate laws intermediate to both of these[18,34]. Since no satisfactory mechanism has been given to explain the validity of the cubic time relationship for scales, it is probable that a true Wagner mechanism is operative, and reports of cubic oxidation may essentially be parabolic with initial deviations. Other investigators[9,35] observed paralinear oxidation rates after extended exposures in the 800°C - 850°C range. Wallwork et al[35] demonstrated that the kinetics of parabolic oxidation could be accounted for by an oxide-metal diffusion model based on scale growth and oxygen solution in zirconium at 850°C. The equation accounting for the mass balance of oxygen at the metal/oxide interface was solved assuming a linear concentration gradient in the

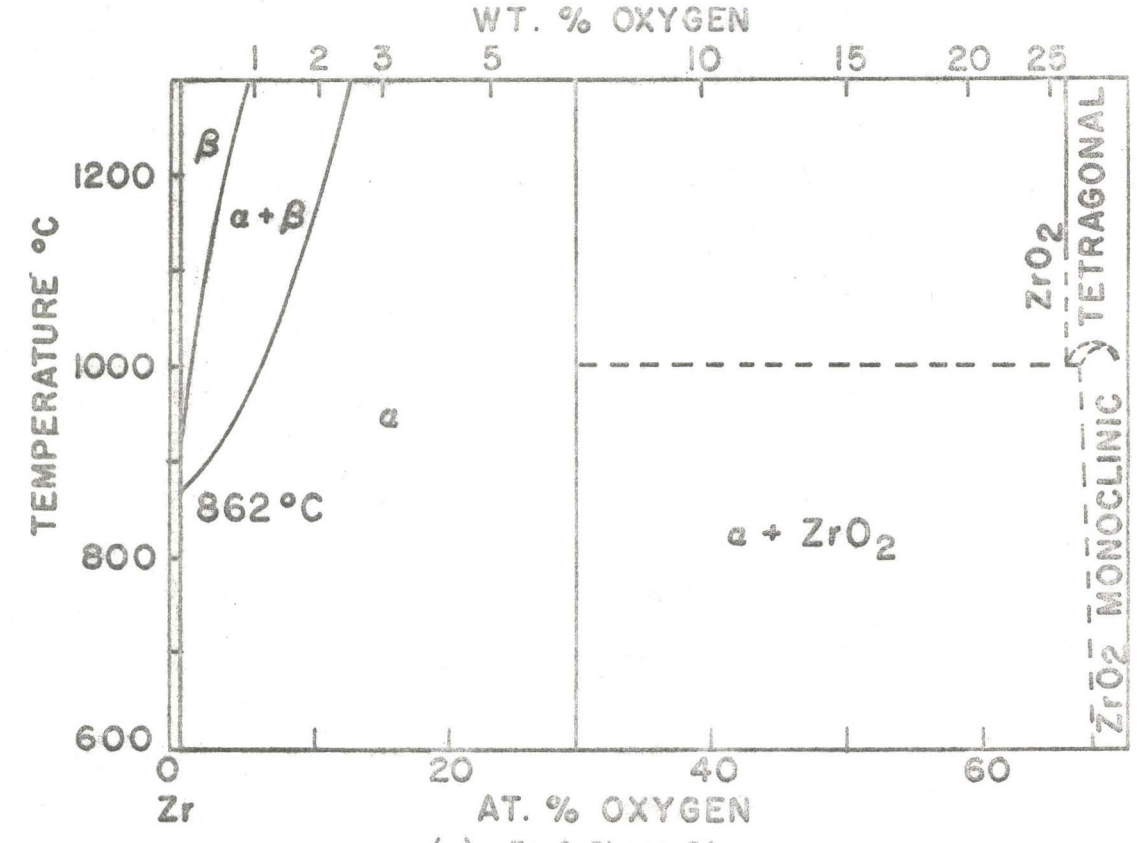

(a) Zr-O Phase Diagram

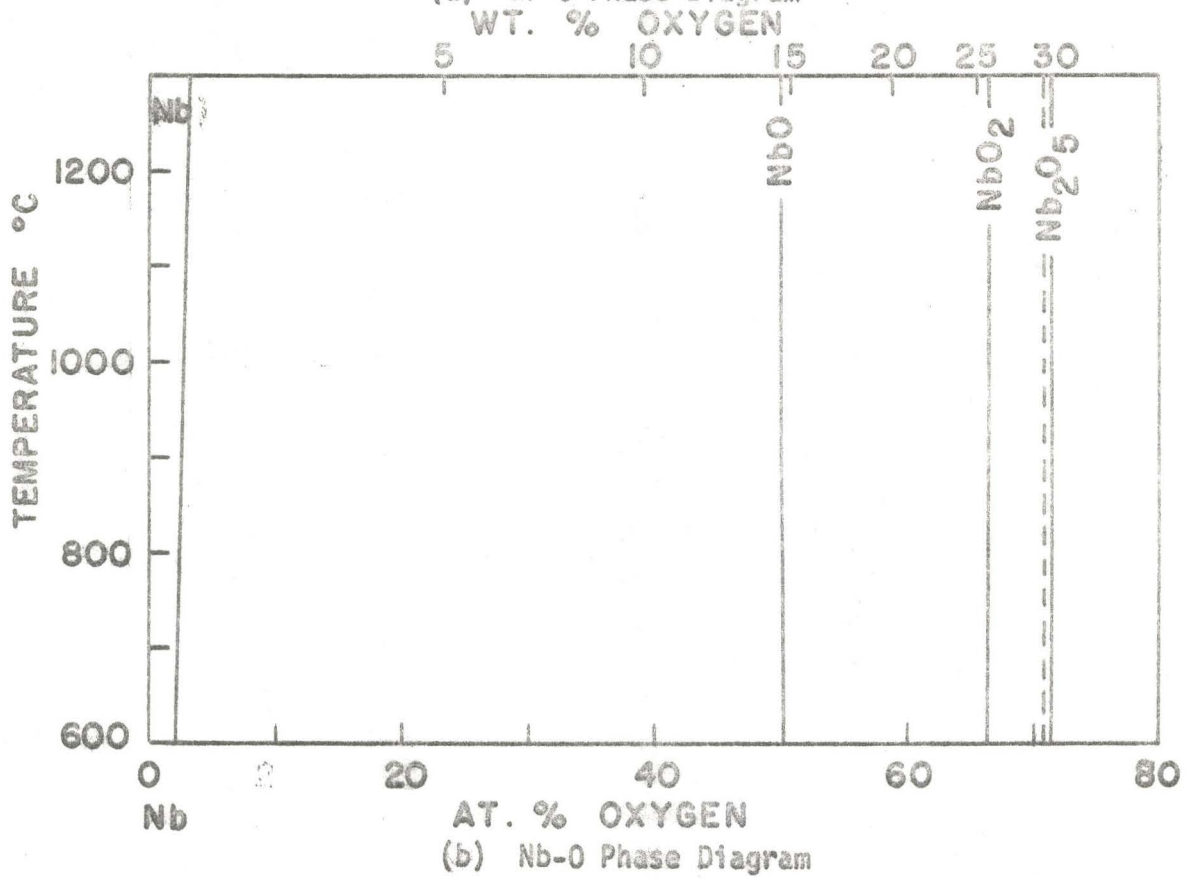

(b) Nb-O Phase Diagram

Figure 1

scale and an error function relationship describing the concentration profile of oxygen in the metal. Solution of the equation yielded:

$$\left(\frac{\Delta m}{A}\right) = \left\{2\gamma_\varepsilon \left(C_{II}^{I} - C_{I}^{II}\right)\sqrt{D_{II}} + 2B_I \sqrt{D_I/\pi}\, \exp\left(-\frac{\gamma^2 D_{II}}{D_I}\right)\right\}\sqrt{t} \qquad (3\text{-}1)$$

C_{II}^{I} and C_{I}^{II} = the oxygen concentrations in the oxide and metal respectively at the metal/oxide interface.

D_{II} and D_I = the oxygen diffusion coefficients in ZrO_2 and α-Zr respectively

t = time

B_I and γ = constants

Thus,

$$\left(\frac{\Delta m}{A}\right) = \left\{k_p(\text{oxide}) + k_p(\text{metal})\right\}\sqrt{t} = K_p\sqrt{t} \qquad (3\text{-}2)$$

where k_p(oxide) and k_p(metal) represent constants in the parabolic relationship for oxide growth and oxygen solution in the metal.

Oxidation of β-Zr has been found to follow a parabolic rate[17,34,36]. Due to the diffusion of oxygen into the metal, a region of α-Zr is stabilized beneath the oxide scale. Rosa and Smeltzer[36] extended the two-phase model for parabolic oxidation of α-Zr to account for the three phases present during oxidation in the β-region. In an analagous manner, diffusion relationships are derived from an oxide-metal model depicting the growth of a scale and an α solid solution respectively, with concurrent solution of oxygen in the β-Zr substrate. Thus,

$$\left(\frac{\Delta m}{A}\right) = \left\{k_p(\text{oxide}) + k_p(\text{alpha}) + k_p(\text{beta})\right\}\sqrt{t} = K_p\sqrt{t} \qquad (3\text{-}3)$$

Zirconia (ZrO_2) is the reaction product which is formed at all temperatures. Lower oxides of zirconium are not known. Zirconia is known to exist in three polymorphic forms: monoclinic, tetragonal and cubic. The cubic is stable at very high temperatures. The low temperature form of ZrO_2 is monoclinic which transforms to the tetragonal form at approximately 1000^oC. The transformation is of a martensitic type and exhibits a hysteresis loop. Some investigators have observed the tetragonal phase during oxidation studies of zirconium. This phase may be stabilized below the transformation temperature due to fine grain size, high compressive forces in the oxide and/or high defect structures. Zirconia is accepted as being oxygen deficient but the extent on the nonstoichiometry of ZrO_2 in equilibrium with oxygen saturated zirconium is not fully known.

The oxidation process is generally believed to occur by the diffusion of oxygen ions through the oxide via anion vacancies. At the oxide/gas interface, anion vacancies and electrons are consumed resulting in the formation of oxygen ions:

$$O_2 + 2\,\square^{=} + 4e^{-} = 2O^{=} \qquad (3\text{-}4)$$

At the metal/oxide interface zirconium ions and oxygen vacancies are formed:

$$Zr = Zr^{+4} + 2\,\square^{=} + 4e^{-} \qquad (3\text{-}5)$$

Oxygen diffusion to the metal/oxide interface results in the formation of ZrO_2 at the interface, a result which has been confirmed by marker studies.

From the data obtained by a number of experimenters, the parabolic rate constant has an approximately constant activation energy of about 36 kcal/mole over the temperature range 400 - 900^oC. For those who report cubic

rate oxidation rates, the data suggests a change in the activation from about 37 kcal/mole below 600°C to about 47 kcal/mole at 600 - 900°C.

For a more extensive review of the literature pertaining to zirconium oxidation, reference is made to the review article recently compiled by Rosa[38].

3.2 Oxidation of Niobium

Not unlike zirconium, the oxidation of niobium has also been studied by numerous investigators. Hurlen[39] made a thorough study in the temperature range 150° - 1000°C with varying oxygen pressures up to atmospheric. Sheasby, Wallwork and Smeltzer[40] carried out investigations at 720° - 825°C while work at temperatures greater than 1200°C has also been done[41].

The Nb-O phase diagram is given in Fig. 1(b). The main oxides of niobium are NbO, NbO_2 and Nb_2O_5. NbO and NbO_2 have negligible ranges of solid solubility while Nb_2O_5 exhibits a limited solubility. NbO is a grey oxide having a cubic structure while NbO_2 is black and possesses a tetragonal structure. Several modifications of Nb_2O_5 exist. γ-Nb_2O_5 is formed from oxidation below about 830°C. At this temperature, a γ-α Nb_2O_5 transition takes place; both the γ and α forms have been indexed according to a monoclinic structure.

Oxidation of niobium below 650°C involves a period of parabolic behaviour followed by a breakaway transition. It is agreed that the parabolic region is a result of dissolution of oxygen in the metal and the formation of suboxides, while breakaway is associated with Nb_2O_5 formation. Nb_2O_5 is very porous and exhibits a Pilling-Bedworth ratio of 2.2 - 2.5. Above

650°C the oxidation rates are essentially linear, however, an initial parabolic region is observed. Lower oxides of the form NbO and NbO_2 may now form rather than the suboxides observed at lower temperatures[39-41]. The initial parabolic oxidation may be partly due to compact NbO_2 formation while again the linear oxidation is associated with the formation of porous Nb_2O_5.

3.3 Oxidation of Zr-Nb Alloys

Kinetic studies on the oxidation of zirconium-niobium alloys has been carried out to a limited extent, and only recently has the open literature contained some information on the oxidation of these alloys. The only ternary phase diagram available is the 1500°C isotherm (Fig. 2). Simms, Klopp and Jaffee[42] studied the oxidation of the Nb-Zr alloys, containing up to 35 a/o Zr, at 600 - 1000°C in air. Nb_2O_5 was the primary oxidation product but an adherent subscale (believed to be NbO or an NbO-type oxide) was observed between the Nb_2O_5 layer and the base metal. Zmeskal and Brey[43] studied the oxidation of Zr-Nb alloys in oxygen at 525°C to 1090°C at a pressure of 200 mm Hg. At 1090°C oxidation of pure Zr and Zr-Nb alloys in the concentration range 60 - 90 w/o Nb was parabolic; those in the 25 - 50 w/o Nb range followed a cubic law with the minimum reactivity occuring in this range. At low Nb contents, the scales were primarily monoclinic ZrO_2 with the mixed oxide, $6ZrO_2 \cdot Nb_2O_5$, to a lesser extent; at high Nb contents the oxide was primarily Nb_2O_5 with smaller amounts of the mixed oxide. $6ZrO_2 \cdot Nb_2O_5$ was detected at all compositions but maximum formation occurred at ~50% Nb. The existence of orthorhombic $6ZrO_2 \cdot Nb_2O_5$ has been indicated by Roth and Coughanour[44].

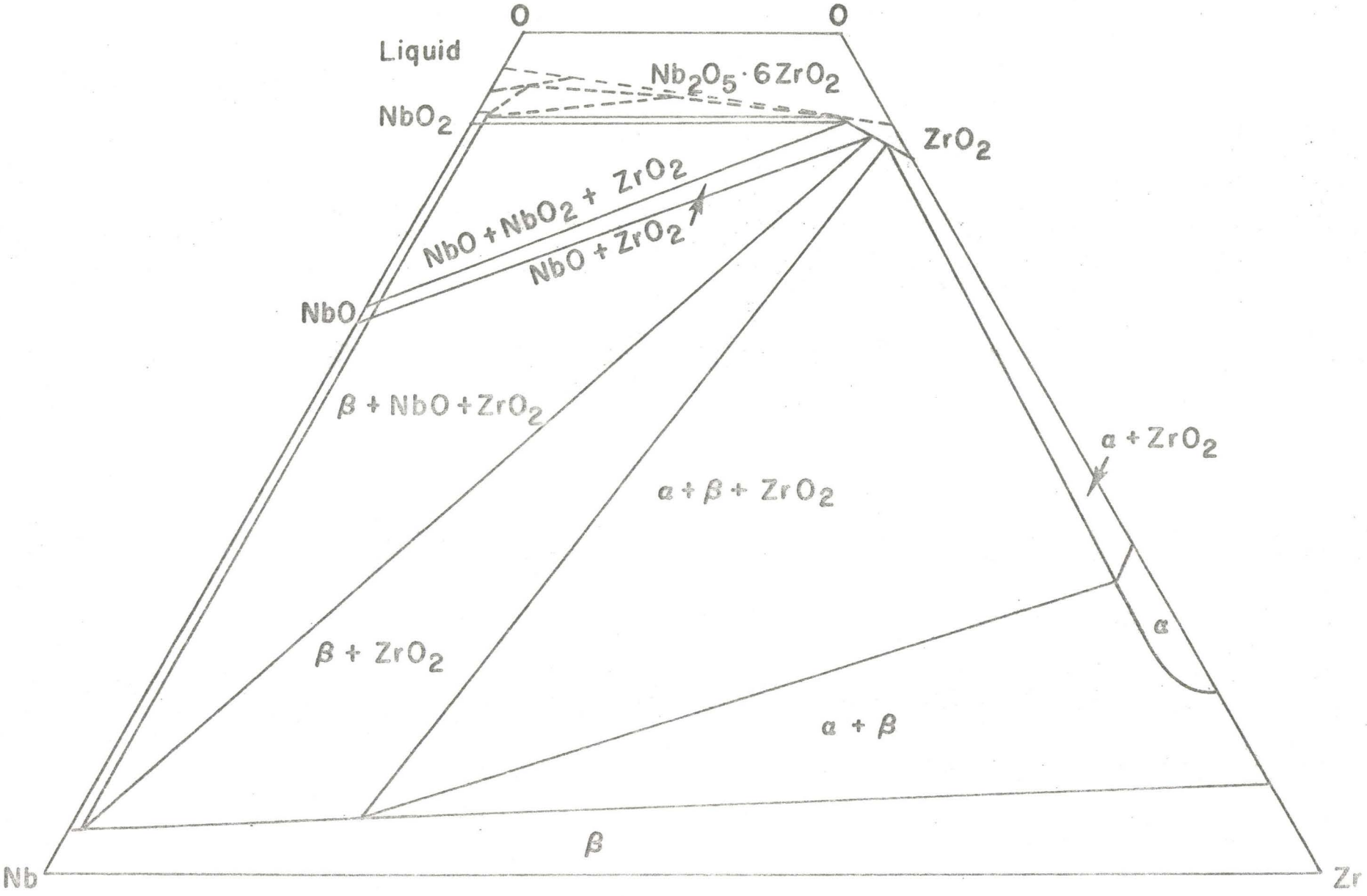

Figure 2. Zr-Nb-O Ternary Phase Diagram (1500°C isotherm)

Rapp and Goldberg[45] in a study of Nb-Zr alloys up to 40 a/o Zr oxidized at 1000°C in oxygen, observed an external scale primarily of Nb_2O_5 with some $6ZrO_2 \cdot Nb_2O_5$ and an internal oxide of ZrO_2 platelets extending from the unoxidized alloy to the outer scale. ZrO_2 platelets resulted from the oxidation of α-Zr platelets which were stabilized in advance of the internal oxidation zone. The formation of $6ZrO_2 \cdot Nb_2O_5$ was believed to be a result of a solid-solid reaction between Nb_2O_5 and ZrO_2. Linear oxidation kinetics were observed for these alloys, with increasing zirconium additions reducing the rate.

Cowgill and Smeltzer[46] reported the oxidation properties of a Zr-2.7 w/o Nb alloy in both martensitic and Widmanstatten structures, of which the martensite oxidized most rapidly. The initial rate was found to be dependent on the volume fraction of martensite present. The major oxidation product was monoclinic zirconia, but the appearance of an extra reflection in the X-ray analysis suggested the possibility of tetragonal zirconia or the mixed oxide, $6ZrO_2 \cdot Nb_2O_5$, being present as well.

Cowgill, Wong and Smeltzer[47] reported the oxidation properties of a Zr-2.7 w/o Nb alloy in the temperature range 870° - 1000°C. Parabolic oxidation was initially observed while a transition to more rapid kinetics followed. Oxidation was characterized by the formation of a region of columnar α precipitates beneath the oxide scale. As above, the oxide was predominantly monoclinic zirconia with tetragonal zirconia or $6ZrO_2 \cdot Nb_2O_5$ as well.

Nomura and Akutsu[18] observed parabolic kinetics for a Zr-2½% Nb alloy in the temperature range 600° - 850°C. Microprobe analyses showed the Nb concentration in the alloy and the oxide were approximately the same.

Recently Guerlet and Lehr[48] studied the oxidation of Zr-Nb alloys in a CO_2 atmosphere. Alloys ranging from 1 - 20 w/o Nb were oxidized at 750° and 900°C. The observed kinetics was intermediate between a cubic law and a parabolic law. Due to the segregated substructure, they believed the Zr and Nb oxidized simultaneously, which created multiphase oxide layers containing principally ZrO_2 and Nb_2O_5. $6ZrO_2 \cdot Nb_2O_5$ was believed to have formed as a result of a solid-solid reaction between the two oxides. The amount of mixed oxide increased with increasing Nb content and decreased towards the metal/oxide interface.

CHAPTER IV

Experimental

4.1 Introduction

In the investigation of metal oxidation, reaction kinetics for the oxidation process have been determined using various methods. Of these, the most simple and direct are the gravimetric, volumetric, manometric and electrometric methods. All are reliable means for weight gain determinations, and have been commonly used by various investigators in kinetic studies.

The thermogravimetric method was employed in this investigation for measuring the oxidation rates of the alloy using samples with both rectangular and spherical geometry. The experiments were carried out in an ultra-high purity grade oxygen atmosphere at 760 mm Hg pressure. This grade of oxygen was obtained from Matheson of Canada Ltd. and corresponded to 99.99% O_2.

4.2 Apparatus

The assembly was essentially comprised of four main parts: the oxygen supply system, the argon supply system, the reaction chamber and the semi-microbalance assembly. A schematic diagram of the basic components is illustrated in Fig. 3.

The main feature of the arrangement is the Ainsworth, Type RV, semi-microbalance (1) which allowed a continuous measurement of the weight

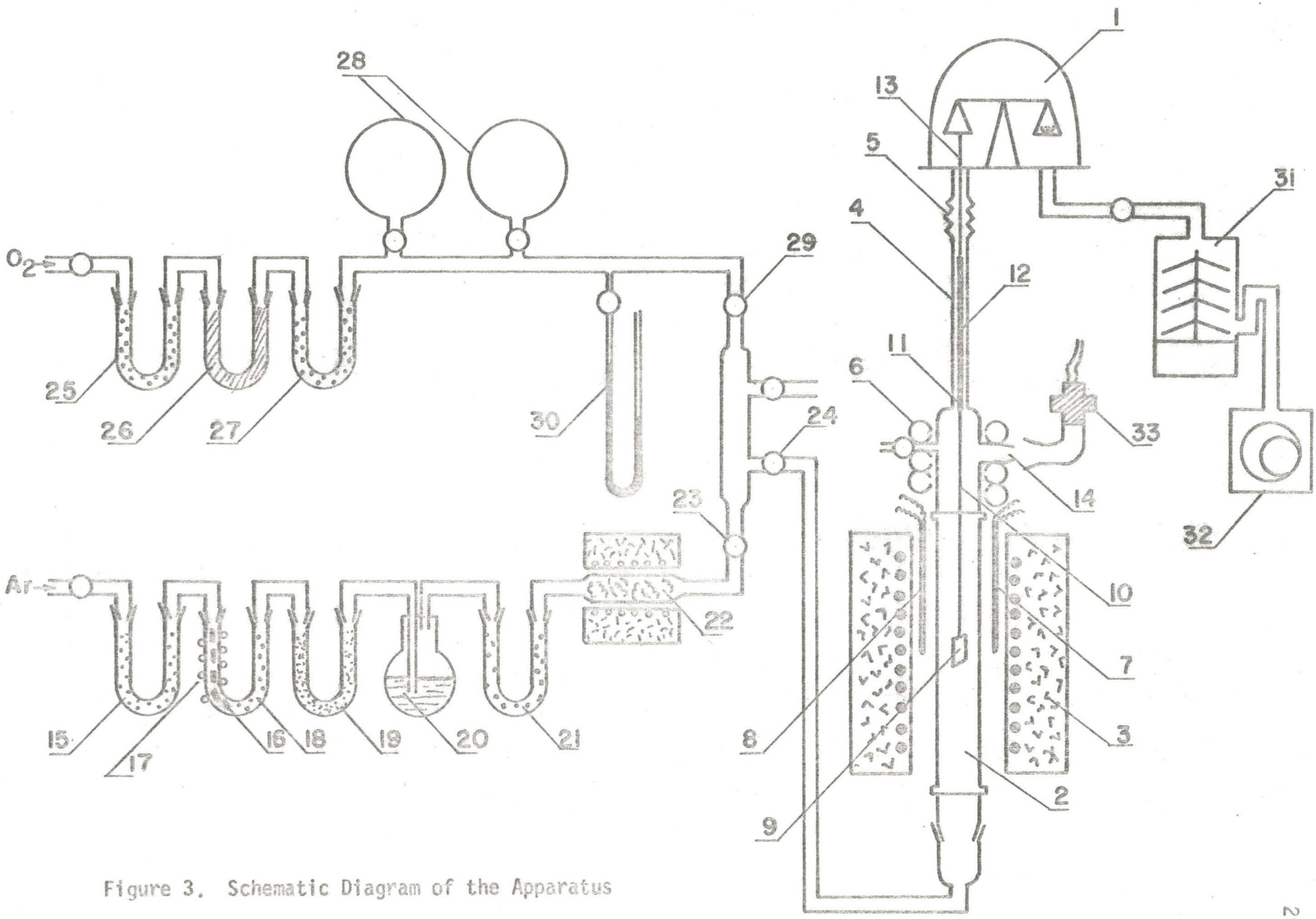

Figure 3. Schematic Diagram of the Apparatus

gain, as the reaction products accumulated on the specimen surface with time. The weight gains were recorded using an Ainsworth, Type AU-1, strip chart recorder. The balance assembly was capable of continuously measuring weight gains up to 400 mg and the sensitivity of the instrument was such that a change in weight of 0.05 mg could be detected.

The reaction chamber was a 30 in. mullite furnace tube (2) of 1 5/8 in. O.D. positioned within a furnace (3) consisting of a 20 in. Kanthal heating element embedded in insulation. Power was supplied to the element by a 2500 VA transformer, and a 3 in. hot zone with a temperature variation of $\pm 2^{o}C$.was maintained within the reaction zone. The reaction chamber was connected to the balance assembly by means of a 25 mm diameter glass tube (4) which was fused to the mullite at one end while the other was connected to the balance with a flexible aluminum metal bellows vacuum joint (5). The region immediately above the fused joint was air cooled (6) such that the specimen could be quenched in this area.

The reaction temperature was measured with a Pt-Pt 10% Rh thermocouple (7) positioned outside the mullite tube at the same level as the specimen in the hot zone within the reaction chamber. This thermocouple was calibrated against another Pt-Pt 10% Rh thermocouple which was placed in contact with a specimen and suspended within the reaction zone. Hence the actual temperature of the sample (i.e., the reaction temperature) could be determined by using the measuring thermocouple (7) and the calibration curve.

The fluctuation of the temperature ($\pm 2^{o}C$) was limited by the sensitivity of the Philips recorder-controller, the thermocouple for the latter (8) being positioned in a similar manner to that of the measuring

thermocouple (7).

The specimen (9) was suspended in the reaction zone by a 0.010 in. Pt-10% Rh wire (10). The wire was attached to an iron rod (11) which in turn was partially enclosed in a pyrex tube (12) that had a bore slightly larger than the diameter of the iron rod. The entire tube, iron rod and wire assembly was suspended from the beam of the balance assembly by means of a nylon thread (13). This arrangement allowed the specimen to be raised or lowered in the furnace by manipulating the iron rod with a magnet from outside the assembly. Specimens were introduced and removed from the assembly by means of a port (14) located in the quenching area of the apparatus.

Commercially pure argon was used as a purging gas. Before entering the system the gas was purified by first passing it through silica-gel (15) for moisture removal and then through BTS catalyst (16) for hydrogen removal, the catalyst being maintained at approximately 250^{o}C with an electric heating tape (17). A result of hydrogen removal was the formation of H_2O, which had to be subsequently removed by further passage through silica gel (18) and magnesium perchlorate (19) in that order, the latter necessary for removal of residual water vapour. The gas then passed through a bubbler (20) of dibutylthalate to a U-tube containing ascarite (21) for the removal of CO_2 and CO. This was followed by passage through heated titanium chips (22) to remove any free oxygen which may be present. The argon was then emitted into the system through stop cocks (23) and (24).

Ultra-high purity oxygen was used as the oxidizing atmosphere and any moisture present was removed by passing the gas through silica gel (25) and then through magnesium perchlorate (26) for removal of residual water

vapour. Any CO_2 and CO was removed with ascarite (27). The oxygen was stored in two large storage bulbs (28) having a total capacity of approximately 8 litres. The oxygen was emitted into the system through stop cocks (29) and (24), and a mercury manometer (30) was located on the oxygen line to fix the pressure of the oxidizing atmosphere.

The whole assembly was evacuated by a Balzers oil diffusion pump (31) coupled with a Balzers two stage rotary vane pump (32). The vacuum was measured from the port (14) using a Balzers ionization gauge (33) which was fixed to the port with a ground glass seal.

4.3 Procedure

It is not the purpose of this section to give a detailed account of the operating instructions but only an approximate description of the operating procedures.

A metallographically polished specimen was placed in the assembly through the port opening and was suspended from the wire by a platinum hook, attached to the sample by a small hole. The port was then closed by connecting the ionization gauge to the opening. The balance beam was then tared with suitable weights and the microbalance was adjusted to record a suitable zero point and maintain the correct sensitivity. The power supply to the furnace was turned on and the air supply to the cooling coil around the quenching area was opened.

The entire system was pumped out with the mechanical pump and this was followed by the admittance of oxygen and argon into their respective lines. Argon was then admitted into the reaction chamber until atmospheric

pressure was attained. The reaction chamber was evacuated again with the mechanical pump. The furnace and balance assembly were again purged with argon and pumped down with the rotary pump for the final time. When the pressure reached a sufficient level, the diffusion pump was turned on, and the pumping was continued throughout the period that the furnace was coming to temperature. A vacuum of less than 10^{-4} mm Hg pressure was considered to be sufficient.

Once the furnace assembly reached the proper temperature and a suitable vacuum was attained, the specimen was carefully lowered into the reaction zone by manipulating the iron rod with the magnet. The sample was held in a vacuum for approximately 15 minutes to ensure that it would be at the reacting temperature before the oxidizing gas was admitted. At the end of that time, the vacuum pumps were isolated from the system and the oxygen gas was admitted into the reaction cell, the balance beam being released at the same moment such that the weight gains could be immediately recorded.

At the termination of the run the balance beam was arrested and the specimen was quenched by rapidly raising it into the air cooled portion of the assembly. After a short time, the sample was removed from the assembly and was mounted and cross-sectioned for microscopic examination. X-ray analysis was done on the reaction product to identify the form of the oxide.

4.4 Materials and Preparations

The Zr-2½ w/o Nb alloy was supplied by the Atomic Energy of Canada Ltd. Material was made available in bar stock form as well as 2 mm thick cold rolled sheet. Rectangular samples were prepared from the sheet while material in the bar form was utilized for the production of spherical specimens.

Rectangular samples for oxidation tests approximately 2 x 1 x 0.2 cm in size were wet abraded on 220, 320, 400 and 600-grit silicon-carbide papers, followed by final polishing on 6 and 1 micron diamond laps, lubricated with kerosene. All six faces of each sample were polished to a 1 micron finish followed by an acetone washing and careful drying. The specimens were then sealed in evacuated quartz capsules and annealed at 1000^{o}C for 1 hour and furnace cooled. The area of each specimen was calculated from values determined by taking the average of three independent micrometer measurements of each sample dimension. Most samples were weighed before and after the oxidation tests.

Spherical samples, used for later experiments, were turned out on a metal lathe to a diameter of approximately 1 cm. This was followed by wet abrasion with silicon-carbide papers, as outlined above, only in this case they were abraded by hand, due to the nature of the sample geometry. Final polishing was done on 6 and 1 micron diamond lap with the aid of a jig, shown in Fig. 4, which was constructed to facilitate the final polishing stages of the spherical samples. The washing, drying and annealing procedures for the spheres were identical to those for the plate samples, as outlined above. The surface areas were calcualted from the diameters of the spheres, the diameter of each sphere being taken as the average value of ten inde-

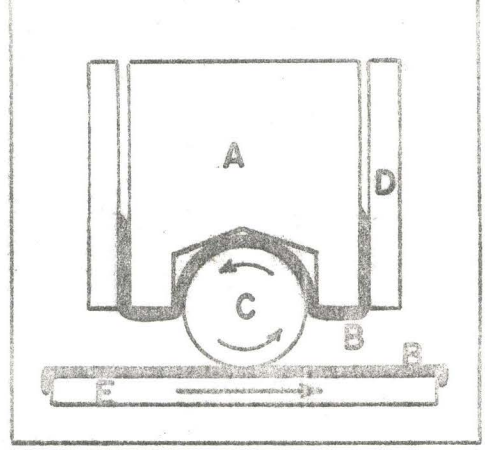

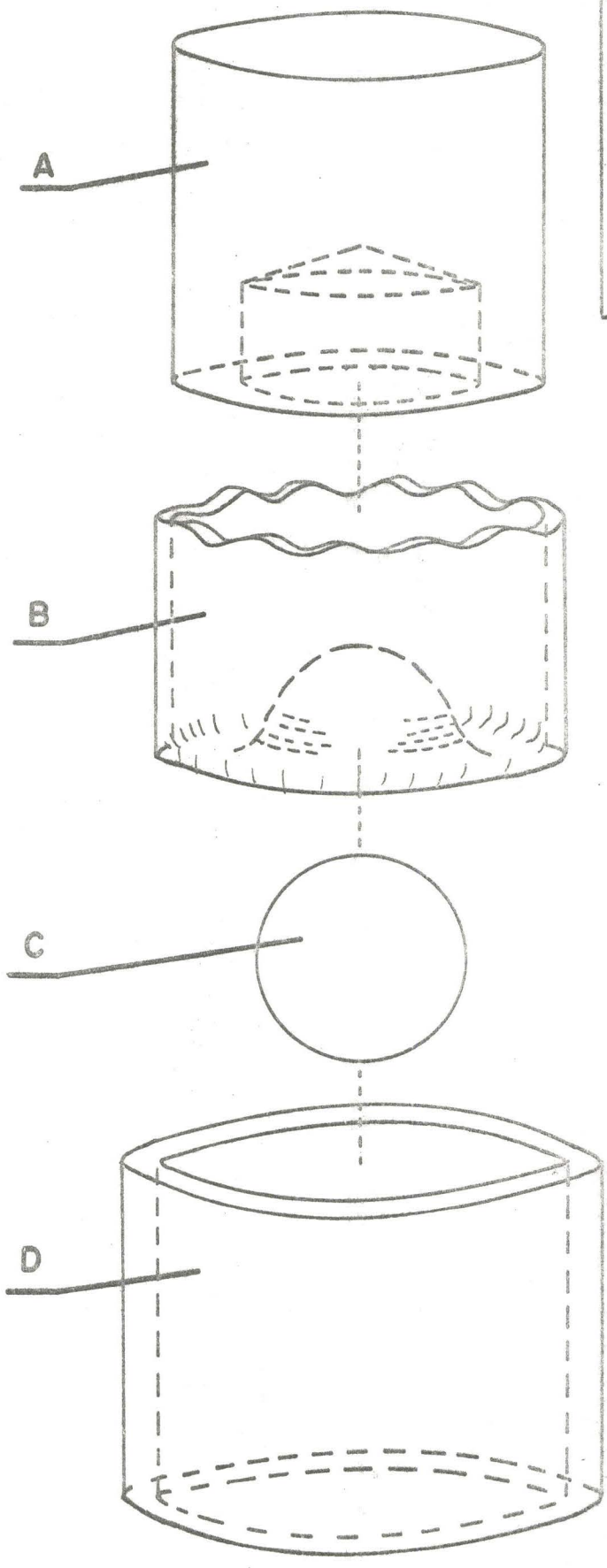

A - LUCITE

B - POLISHING CLOTH

C - SPHERICAL SPECIMEN

D - PERSPEX RING

E - ROTATING WHEEL

Figure 4. Diagram of the Polishing Jig

pendent micrometer measurements. All samples were weighed before and after the oxidation tests.

The oxidized samples were mounted in araldite self-setting epoxy resin, a very hard resin which helped to reduce the surface relief which arises in polished cross-sections due to various constituents of different hardness. Polishing was initially carried out on 220, 320, 400 and 600-grit silicon-carbide abrasive papers using kerosene as a lubricant. The kerosene lubricant minimizes oxide porosity, due to the oxide chipping out, which is induced when lubricated with water. Final polishing at the 6 and 1 micron stages was carried out on nylon polishing cloths impregnated with diamond paste. Nylon, being a napless cloth, also helped to minimize any surface relief. For more detailed metallographic examination of the oxide at high magnifications, it was necessary to carry out the final polishing stages down to a ¼ micron finish using silk polishing cloths, producing an extremely flat and pore-free oxide cross-section.

For metallographic examination, the polished samples were etched in an aqueous solution of 30 v/o H_2SO_4, 30 v/o HNO_3, and 10 v/o HF. Measurements of oxide thicknesses, etc., were made on cross-sections of polished and etched specimens using a standard metallographic microscope equipped with a filar micrometer eyepiece.

X-ray determinations were made of both the light and dark scale constituents. The oxide was scraped off the reacted samples and ground to a fine powder. Samples were prepared for the Debye-Scherrer powder method of X-ray analysis as well as for recording X-ray scanning diffractometer measurements. Nickel-filtered copper K_α radiation was used in the analyses. X-ray diffractometer measurements were also done on the oxide at the metal/oxide

interface. The metal was dissolved away from the oxide in the etching solution at a slightly elevated temperature, exposing the underside of the scale, which was subsequently examined with X-rays. This type of X-ray examination was carried out only on material oxidized in the β region for reasons which will be pointed out later.

Variations in the concentration of Zr and Nb in different phases present in the underlying metal were qualitatively examined using an Acton electron probe microanalyser. Samples for the micro-probe were prepared using the polishing technique outlined previously to attain a flat surface. The specimens were unetched and it was necessary to deposit a thin layer of carbon on the surface to eliminate any build up of charge on the sample due to the non-conducting nature of the oxide.

A Cambridge scanning electron microscope was used to a limited extent to distinguish between various phases in the oxide and underlying metal, which were undistinguishable under a conventional optical microscope. Samples prepared for conventional optical microscopy were used, the different phases being resolvable in the SEM due to the difference in reflectivities between various phases and differences in the rates of attack by the etchant producing a surface relief. The scanning electron microscope was also used to examine the topography of the oxide scales.

CHAPTER V

Results and Observations

5.1 Introduction

The results of the oxidation tests are reported in this section in basically two parts. The first part deals with the experimental results obtained in the temperature range 650°C to 991°C, using plate samples. The kinetic data are presented in the form of oxidation rate curves determined from continuous weight gain measurements. From the Zr-Nb phase diagram appearing in Elliott's[49] text (see Fig. 5), it is evident that the above temperature range extends from the two phase, $\alpha + \beta$, region to the high temperature, β phase, region. The oxidation rate constants, are plotted in an Arrhenius type plot, to show the variation in the rate of oxidation between the β and the $\alpha + \beta$ regions. Oxidation of the alloy in the β region produced the formation of a unique columnar structure consisting of plates of the α phase extending inwards into the metal substrate from the oxide/metal interface. Further investigations were focused on the formation and growth of the oxide and the corresponding columnar alloy microstructure in the high temperature region. Subsequently the second part of this section concerns the results obtained from oxidizing Zr-2½ w/o Nb spheres at 1000°C. Spherical specimens were used to extend the range of parabolic behaviour by retarding the transition to breakaway, which is promoted along the sharp edges of plate samples. The results of the oxidation tests are presented in conjunction with continuous weight gain determinations,

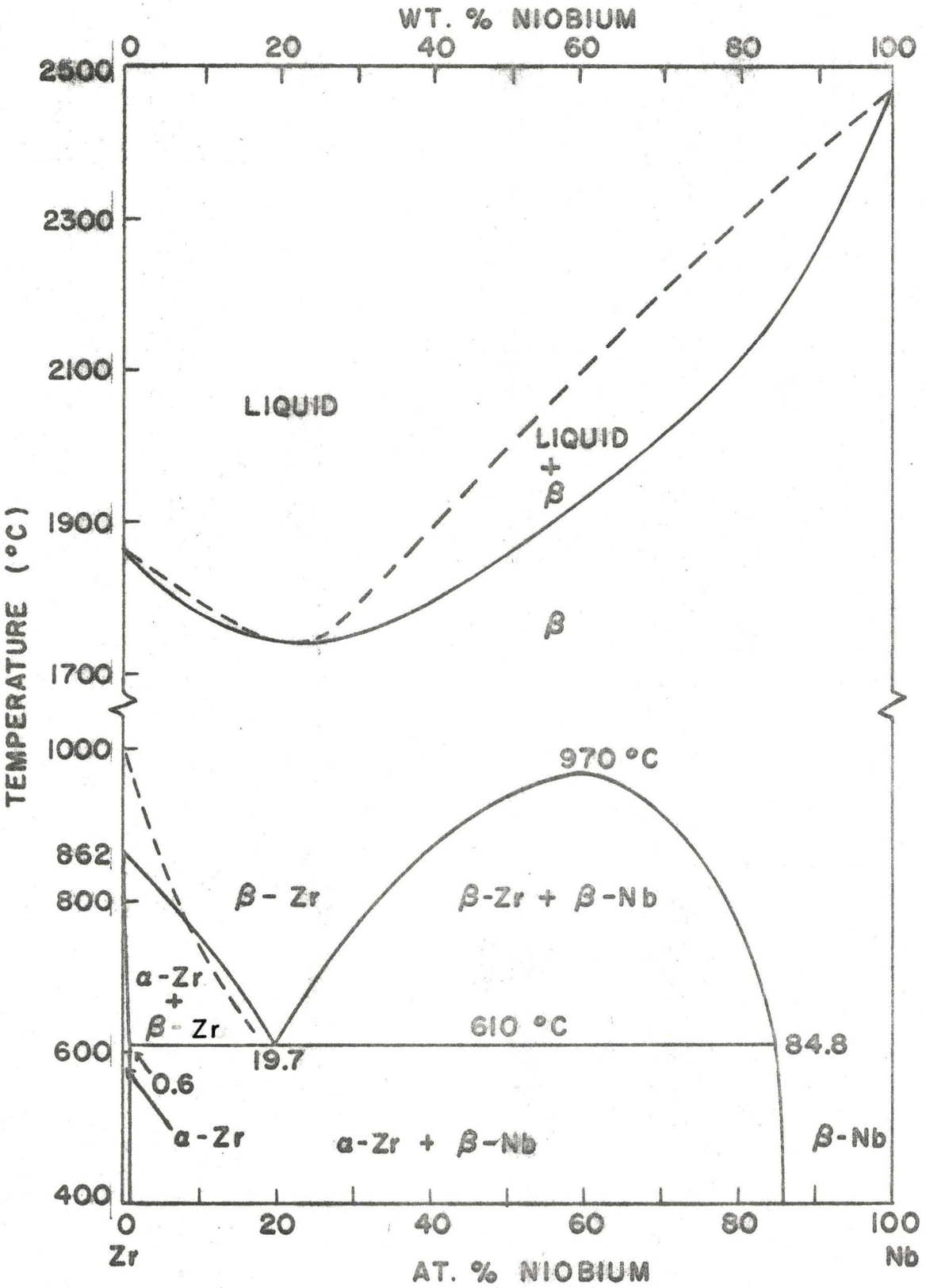

Figure 5. Zr-Nb Phase Diagram

metallographic observations and microscopic measurements.

5.2 Zr-2½ w/o Nb Alloy Prior to Oxidation

Fig. 6 is a micrograph of the structure of a Zr-2½ w/o Nb alloy which has been annealed for 1 hour at 1000°C and subsequently furnace cooled. This structure is typical of the alloy samples prior to their exposure in an oxidizing atmosphere at elevated temperatures. Furnace cooling material from 1000°C resulted in the β-cooled structure of coarse acicular α-grains. This structure is readily apparent from the phase diagram.

5.3 Oxidation Measurements at 991°C and 937°C

The oxidation rate curves for samples oxidized at 991°C and 937°C are shown in Figs. 7 and 8. These are plots of the weight gain due to uptake of oxygen, in mg/cm^2, versus the oxidation time in hours. The curves at both temperatures exhibit a region of decreasing rate of oxygen uptake at short oxidation times followed by a region of rapidly increasing oxidation rate at longer exposures. Corresponding plots of the weight gain versus the square root of the oxidation time are shown in Figs. 9 and 10. The straight line portion of these curves indicate that oxidation behaves parabolically during short exposure times; however, at longer times the curves exhibited a breakaway transition leading to more rapid reaction kinetics. At 991°C the parabolic region extended for approximately 2.5 hours as compared to approximately 4 hours at 937°C. Table I gives the values for the parabolic rate constants, k_p, calculated by linear regression from the straight line portions of the parabolic plots. It can also be seen from the form of the curves that after the transition, breakaway occurred at a faster rate at

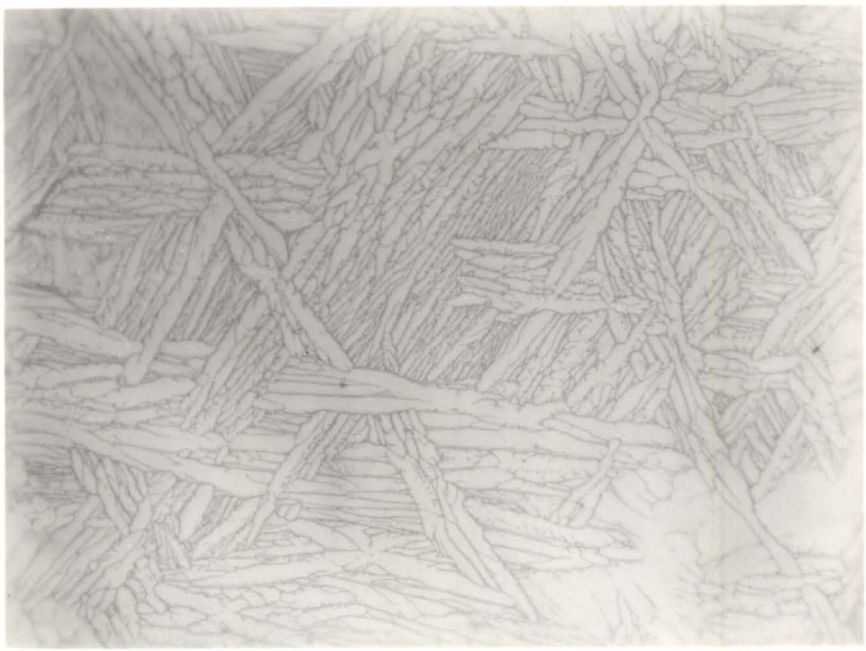

Figure 6. Microstructure of the Alloy Prior to Oxidation (Magnification 400X)

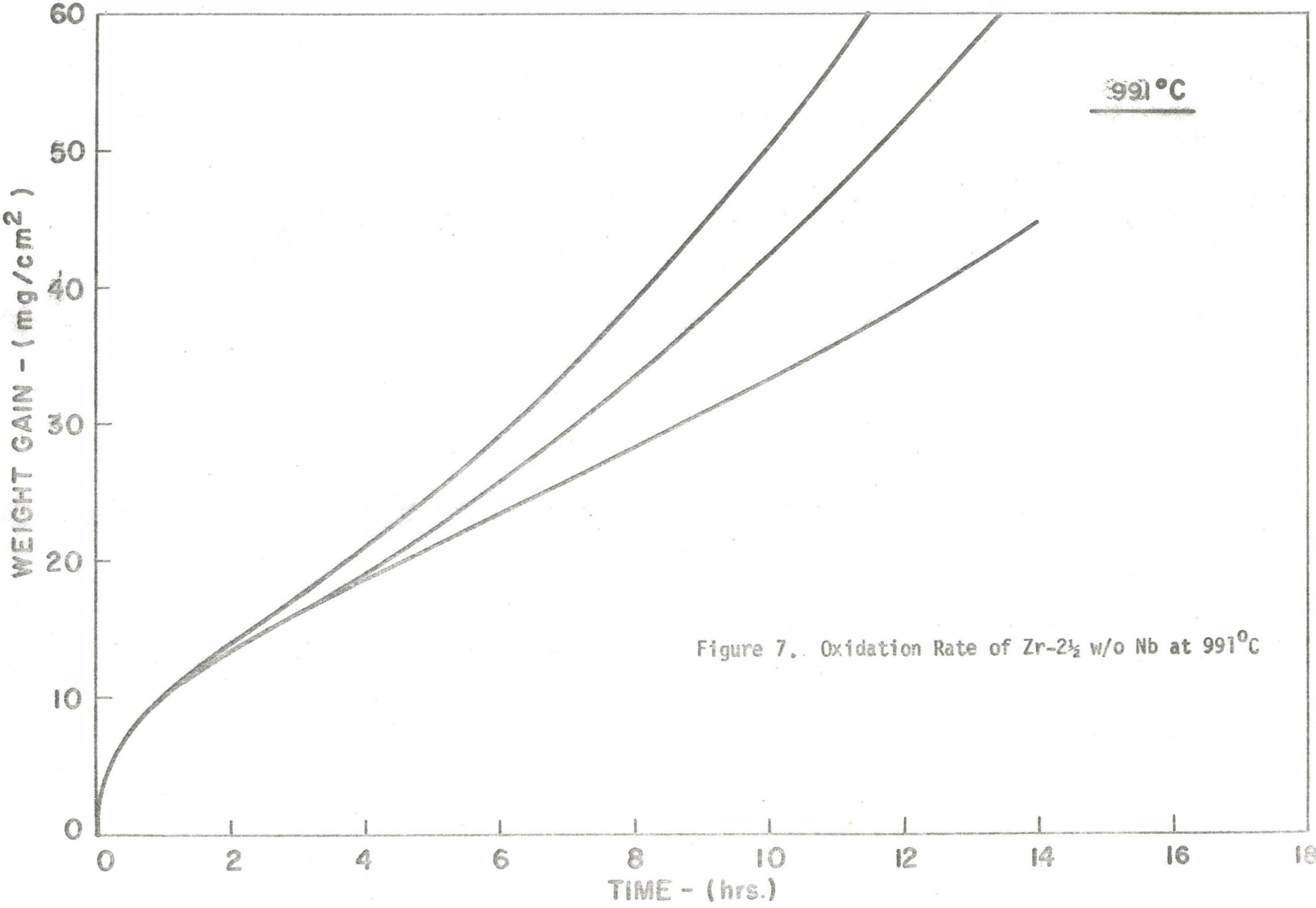

Figure 7. Oxidation Rate of Zr-2½ w/o Nb at 991°C

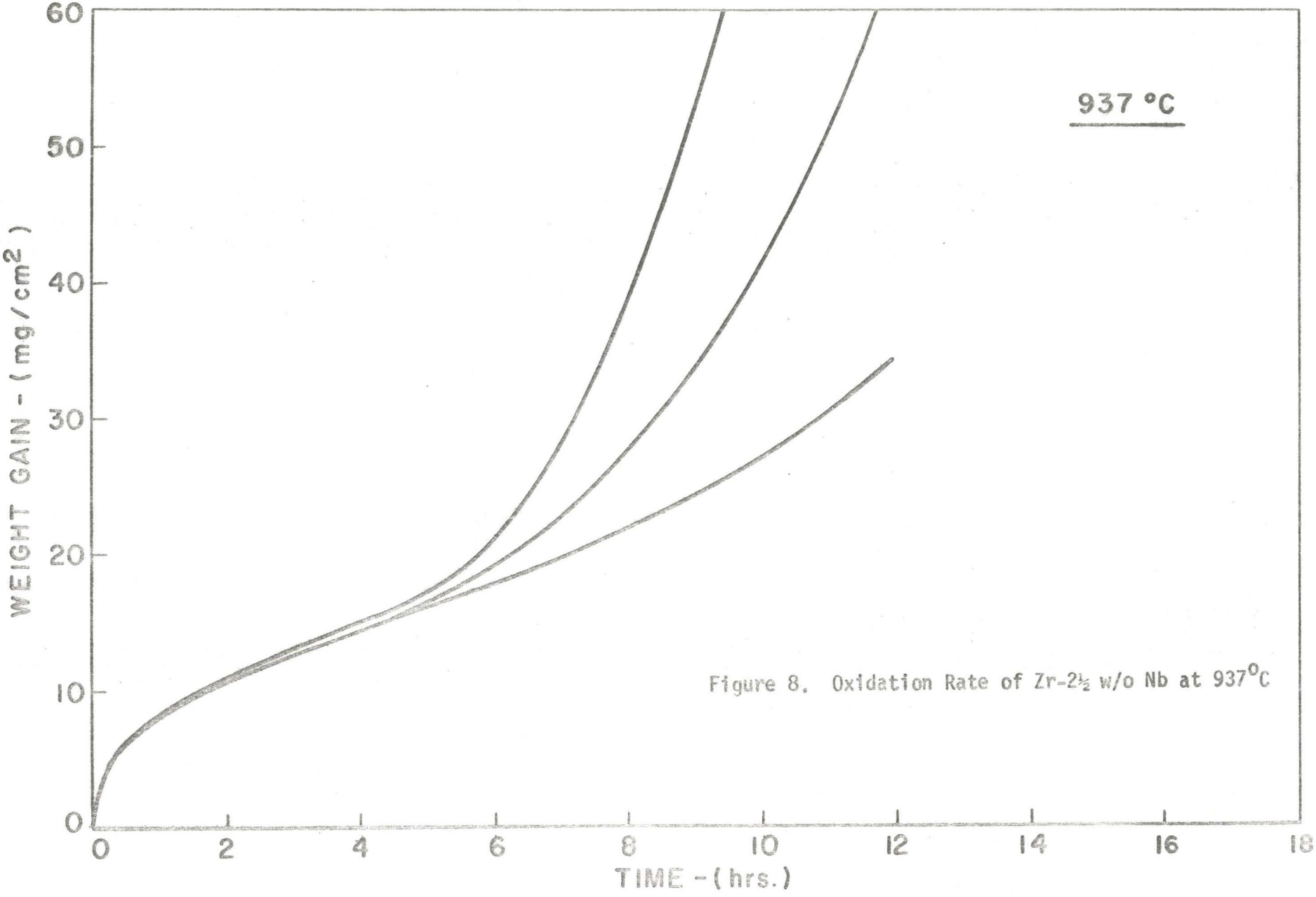

Figure 8. Oxidation Rate of Zr-2½ w/o Nb at 937°C

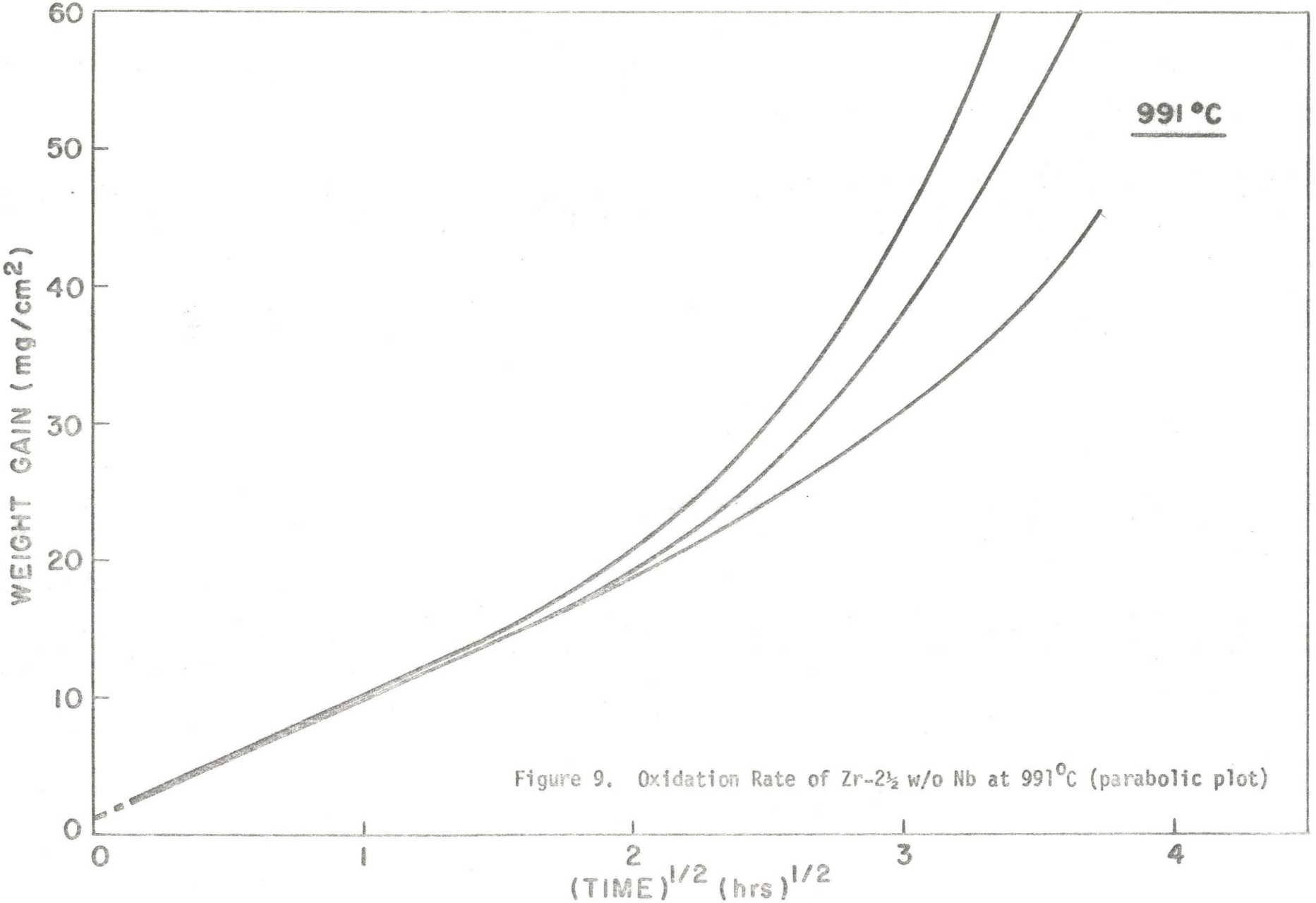

Figure 9. Oxidation Rate of Zr-2½ w/o Nb at 991°C (parabolic plot)

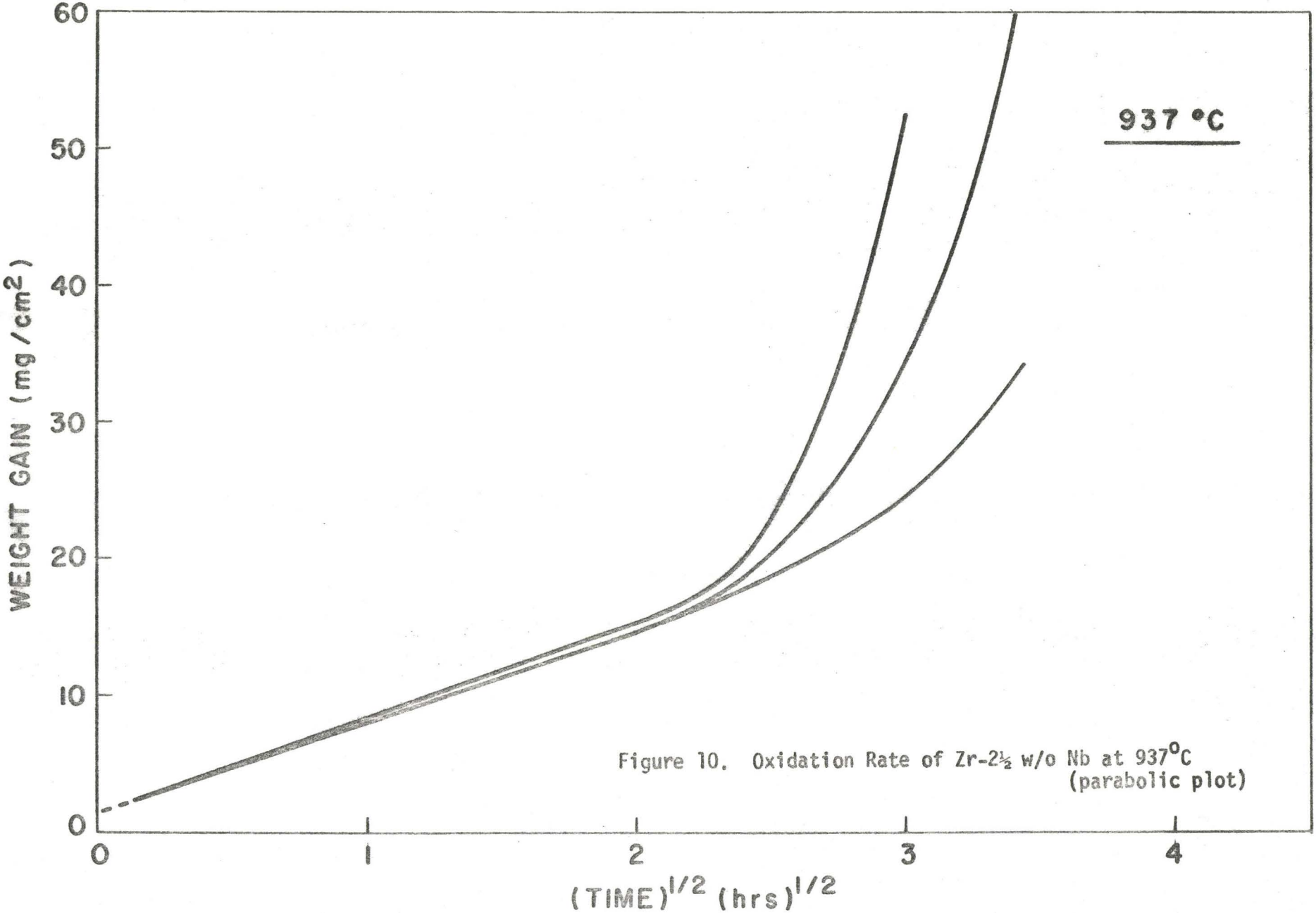

Figure 10. Oxidation Rate of Zr-2½ w/o Nb at 937°C (parabolic plot)

937°C than at 991°C.

After the oxidation tests, most samples were severely deformed due to the long exposure times resulting in the formation of gross amounts of oxide. All samples were characterized by the formation of a white brittle oxide along the edges and corners while the remainder of the surface was primarily covered by a grey adherent oxide. Although the majority of white oxide was concentrated around the edge portions of the samples, some was observed at localized areas within the region predominantly covered by grey oxide. Fig. 11 are micrographs taken with a S.E.M., of the surface of a sample after oxidation at 991°C, and are characteristic of the oxide topography of samples oxidized at 937°C as well. The micrographs clearly show both the grey and the white oxide forms that are present in these temperature ranges, as well as the white oxide penetrating into the region of grey oxide. The compact adherent nature of the grey oxide is clearly evident; in contrast, the white oxide is heavily cracked, with large fissures, running parallel to one another. The largest and deepest fissures were concentrated in the scale along the edges of the samples. The resulting breakaway kinetics occurred at a more rapid rate at 937°C.

5.4 Oxidation Measurements from 885°C to 650°C

Figs. 12 through 14 are the oxidation curves obtained for samples oxidized in the temperature range 885°C to 650°C. During the early periods of exposure a continually decreasing rate of oxygen uptake was observed up to a point at which there was a transition to a more rapid reaction kinetics. Plots of the weight gain versus the square root of time yield straight lines over short exposure times indicating that the oxidation rate behaves para-

Figure 11. Topography of Sample Oxidized at 991^{o}C for 12 hours. (Magnification 20X)

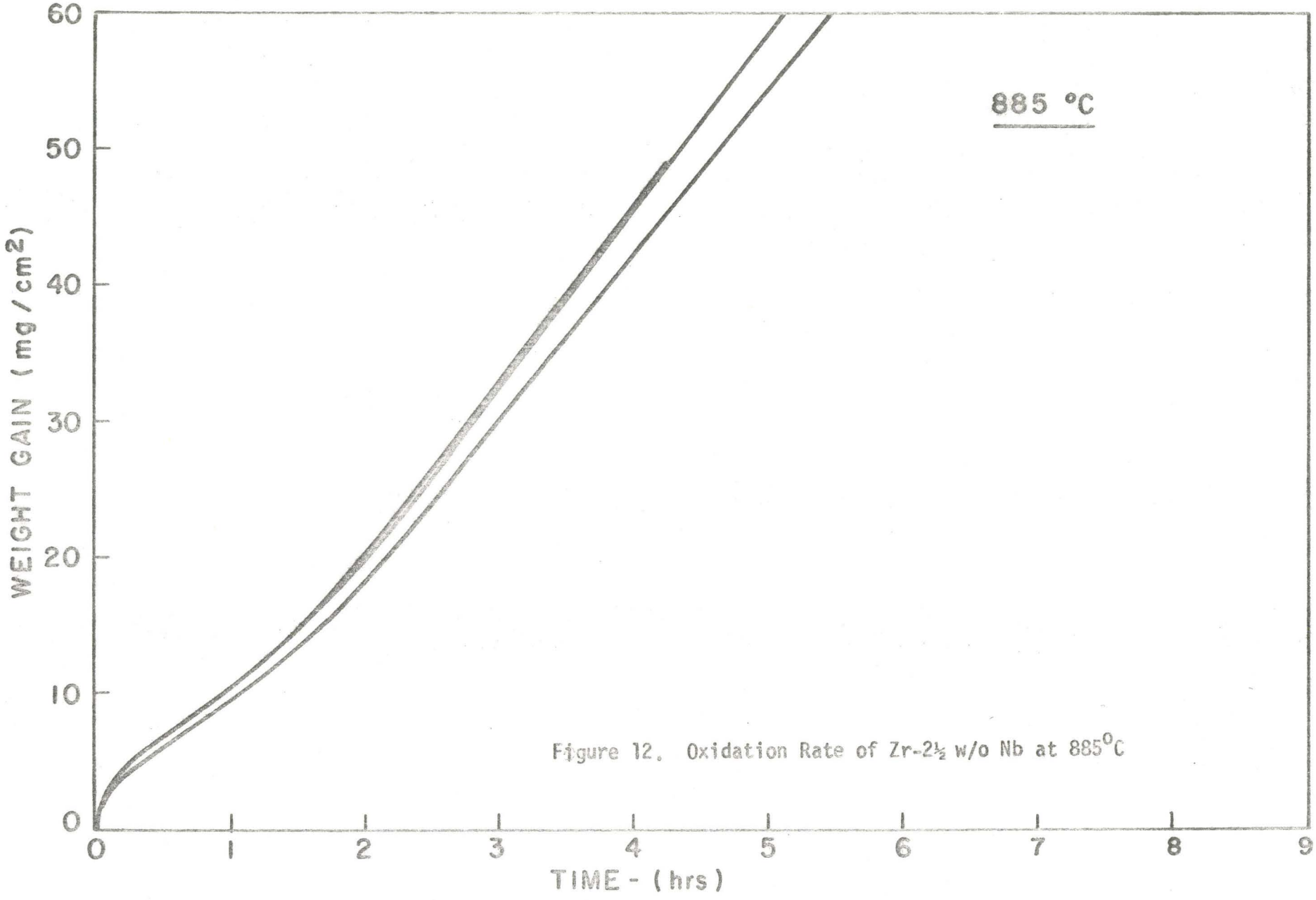

Figure 12. Oxidation Rate of Zr-2½ w/o Nb at 885°C

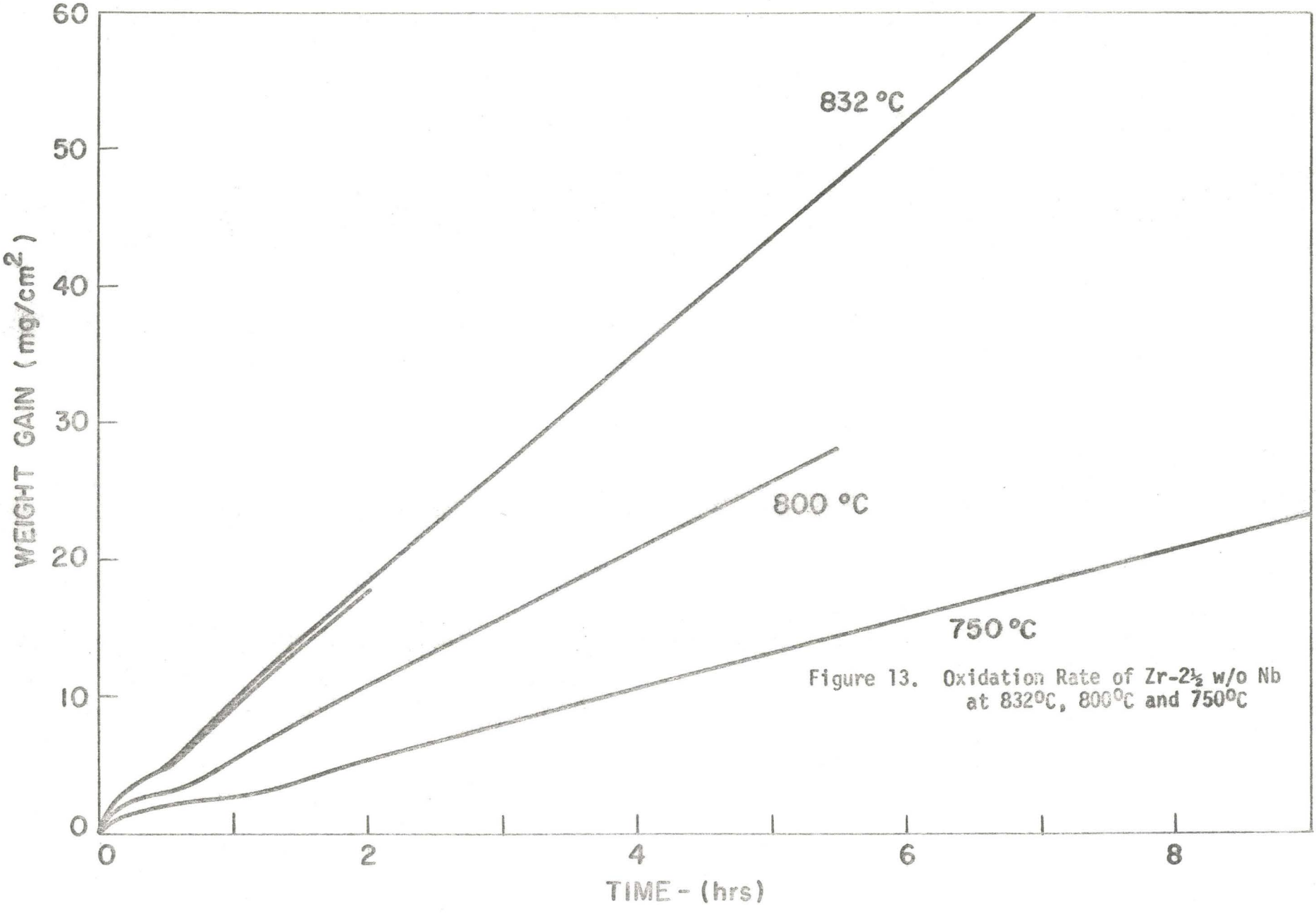

Figure 13. Oxidation Rate of Zr-2½ w/o Nb at 832°C, 800°C and 750°C

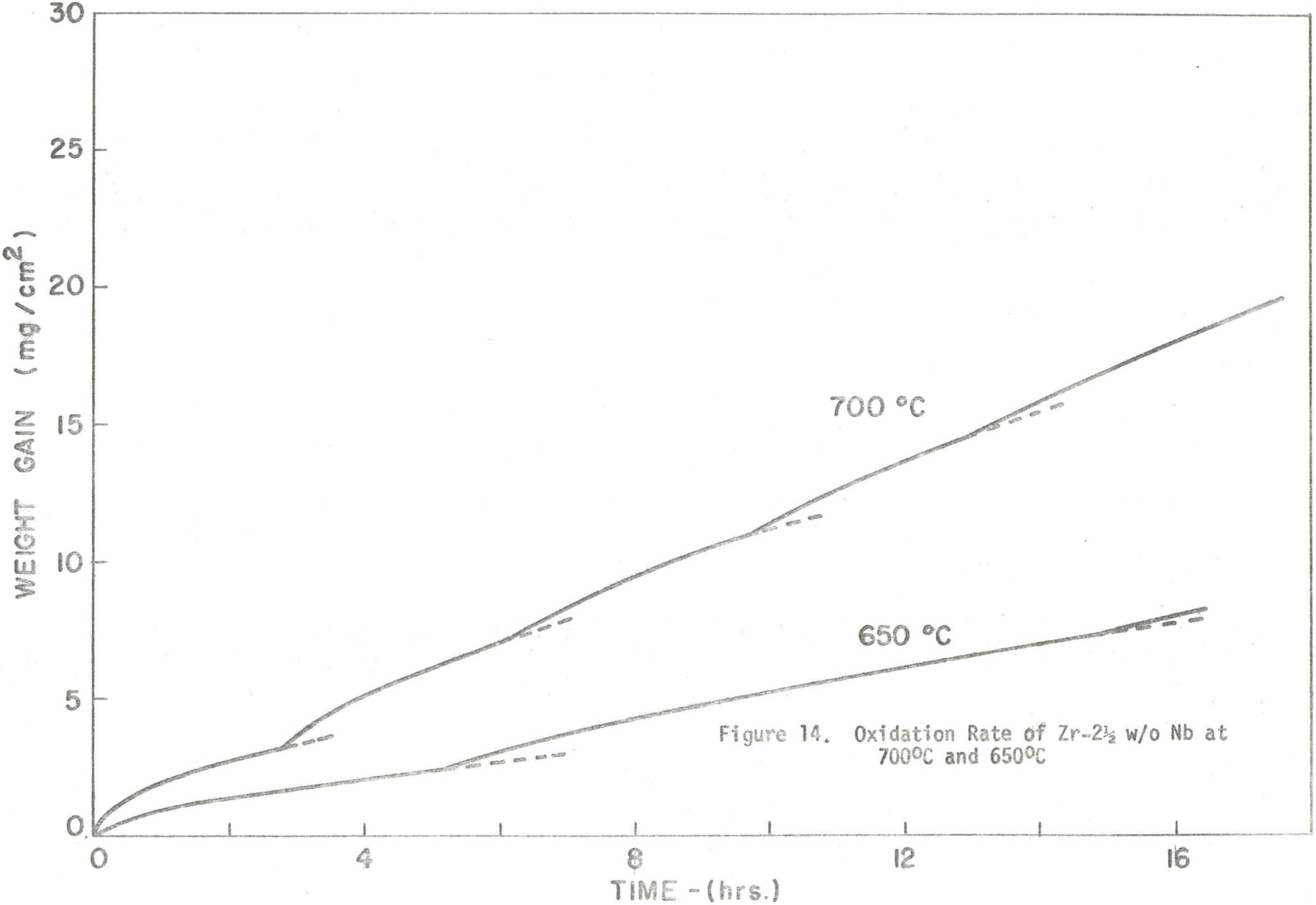

Figure 14. Oxidation Rate of Zr-2½ w/o Nb at 700°C and 650°C

bolically during the early stages of the reaction. These plots are shown in Figs. 15 through 17. From these parabolic plots it may be seen that the region of parabolic reaction kinetics, for samples oxidized at 885°C, extends up to approximately ¼ of an hour before the transition takes place, while the initial period of parabolic behaviour prior to the transition increases up to approximately 3 hours for those reacted at 650°C. The parabolic region increases respectively with decreasing reaction temperature. The values of k_p were determined from the slopes of the linear regions of the parabolic plots by the method of linear regression. These values are given in Table I.

In the temperature range from 885°C to 750°C, the transition that occurred was that from a parabolic rate at short times to essentially a linear rate at longer times. From the reaction rate curves it can be seen that the linear rate decreases with decreasing temperature. At 700°C and 650°C however, the transition was not to a linear rate but to periodic variations in the uptake of oxygen which yielded discontinuities in the oxidation rate curves in these regions. More of these discontinuities appeared at 700°C than at 650°C, the duration of the oxidation tests being approximately the same at both temperatures. In particular, there were approximately 3 times as many at the higher temperature.

In the entire temperature range from 885°C to 650°C, the only reaction product that was visible at the termination of all the tests was the white form of the oxide. Fig. 18a are micrographs of plate samples which are typical of the samples oxidized in the low temperature range. Fig. 18b shows the topography of the oxide scale for a sample oxidized at 885°C. Severe cracking can be observed over the entire area. Smaller secondary

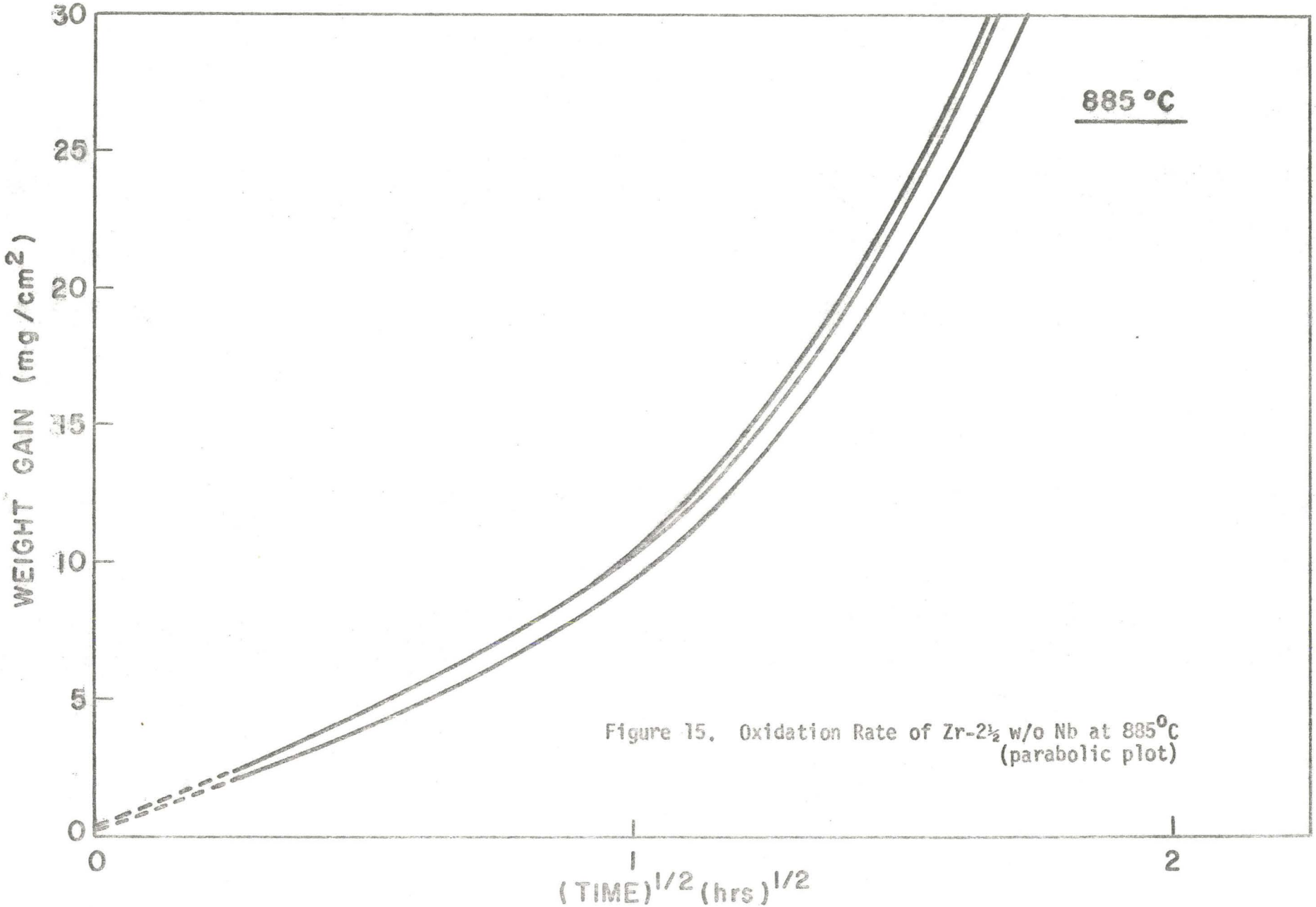

Figure 15. Oxidation Rate of Zr-2½ w/o Nb at 885°C (parabolic plot)

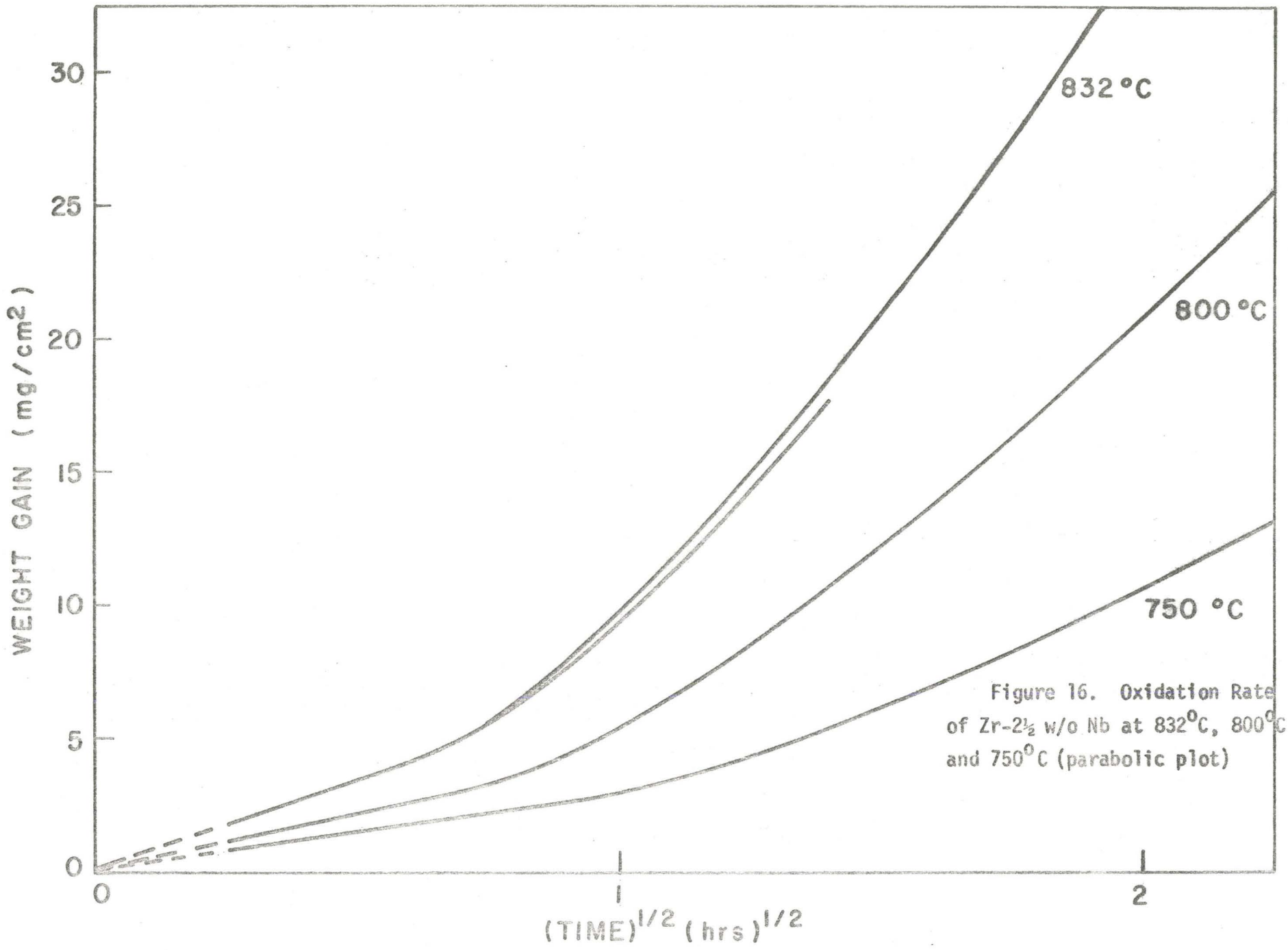

Figure 16. Oxidation Rate of Zr-2½ w/o Nb at 832°C, 800°C and 750°C (parabolic plot)

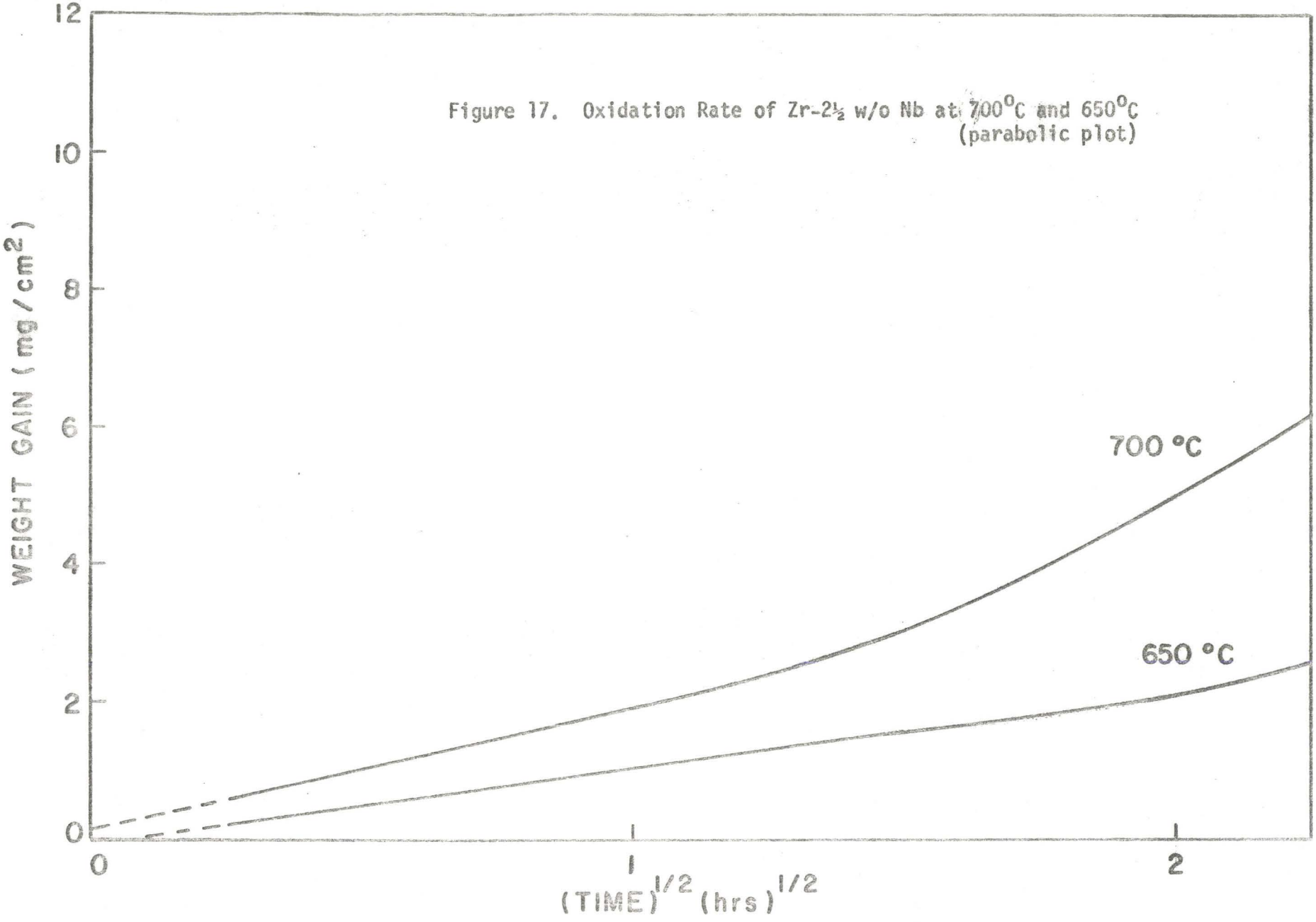

Figure 17. Oxidation Rate of Zr-2½ w/o Nb at 700°C and 650°C (parabolic plot)

885°C
6 hr.

832°C
7 hr.

Figure 18(a). Micrographs of Oxidized Plate Samples
(Magnification 4X)

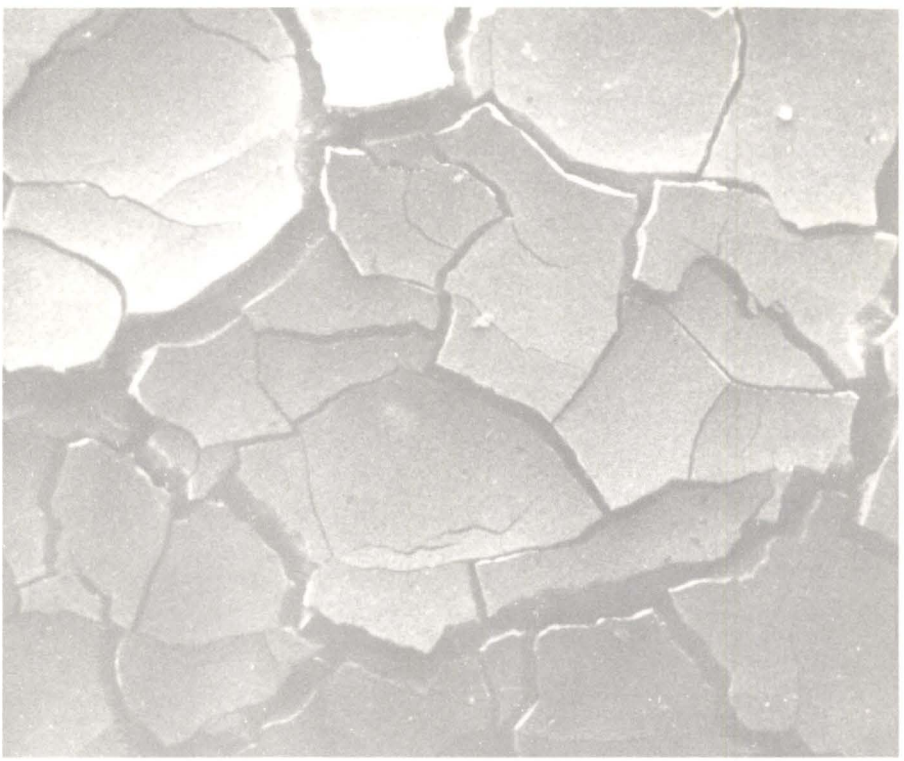

Figure 18(b). Topography of Sample Oxidized at 885°C for 6 hours (Magnification 33X)

fissures appear within the grain-like structure produced by the network of larger initial cracks.

5.5 X-ray Measurements

X-ray analyses were carried out on both the white and grey forms of the reaction product using the Debye-Scherrer powder method. The powder patterns of both forms of the oxide were identical. X-ray measurements were also obtained using the scanning X-ray diffractometer. CuK_α radiation was used on samples of powdered oxide mounted on glass slides with a suitable binding agent. The calculated d-spacing values along with the intensity ratios are given in Table II, with corresponding values for d and the intensity ratios for monoclinic zirconia, obtained from the A.S.T.M. X-ray data file.

The calculated d-values obtained for this particular oxide compare very well to those observed for a monoclinic structure with the exception of one d-value, namely 2.970 Å, which does not correspond to any monoclinic reflections. Thus the reaction product is predominantly monoclinic ZrO_2, but the reflection at 2.970 Å suggests the possibility of some other form of ZrO_2 or a mixed oxide being present. It was also observed that the calculated d-values were slightly larger than those reported for a monoclinic structure.

The calculated d-values obtained for the oxide at the metal/oxide interface for samples oxidized in the β-region appear in Table III. All of the observed d-values corresponded to those observed for monoclinic ZrO_2. The peak at d = 2.970 Å which was observed when the scale was examined

in powder form was not present when analysed in this manner. The observed intensity ratios did not all correspond to those given in the A.S.T.M. Powder Data File for monoclinic ZrO_2.

5.6 Oxidation Measurements at 1000°C

Oxidation measurements at 1000°C were carried out using spherical samples. Typical samples which have been oxidized are shown in Fig. 18c. Since further study was to be focused on the metal substructure during parabolic oxidation, the spheres were used to retard the transition to breakaway kinetics which occurred after a period of short parabolic behaviour using the plate samples.

The oxidation rate curve for a spherical sample oxidized at 1000°C is given in Fig. 19, the duration of the test being 23 hours. The form of the curve is similar to those obtained for plate samples; a region of parabolic oxidation behaviour followed by a transition to more rapid reaction kinetics. However, it can be seen that the edge effect has been eliminated and the parabolic region extends for a longer period of time. From the parabolic plot in Fig. 20 we see that the region of parabolic behaviour extends for at least 12 hours before breakaway occurs. The k_p at 1000°C, calculated from the slope of the parabolic plot is given in Table I.

In the series of static oxidation tests at 1000°C each sample was weighed before and after oxidation. Samples were oxidized for 1, 2, 4, 8 and 16 hours respectively. The weight gains per unit area were calculated and are presented in Figs. 19 and 20 as well. It can be seen that the results of the static tests agree quite well to the oxidation rate curve obtained by continuous weight gain measurements.

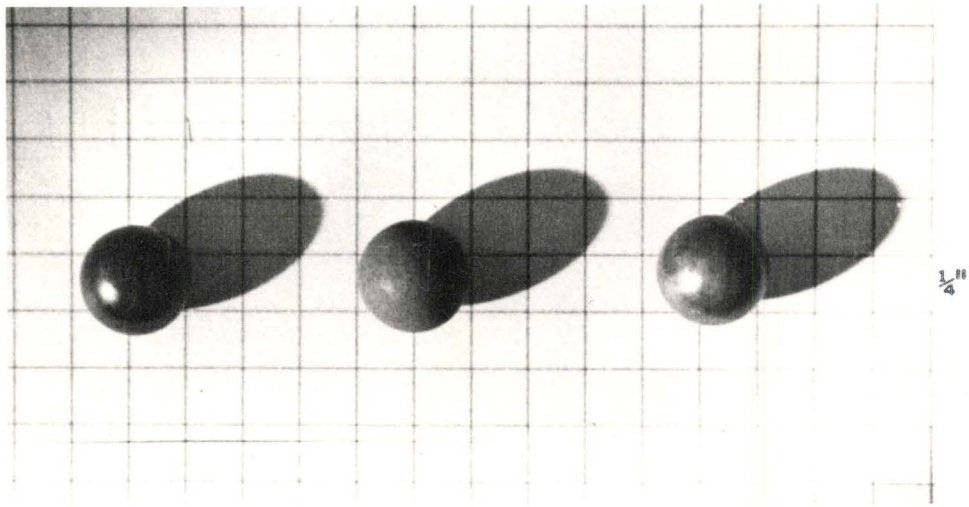

Figure 18(c). Spherical Samples Oxidized at 1000°C

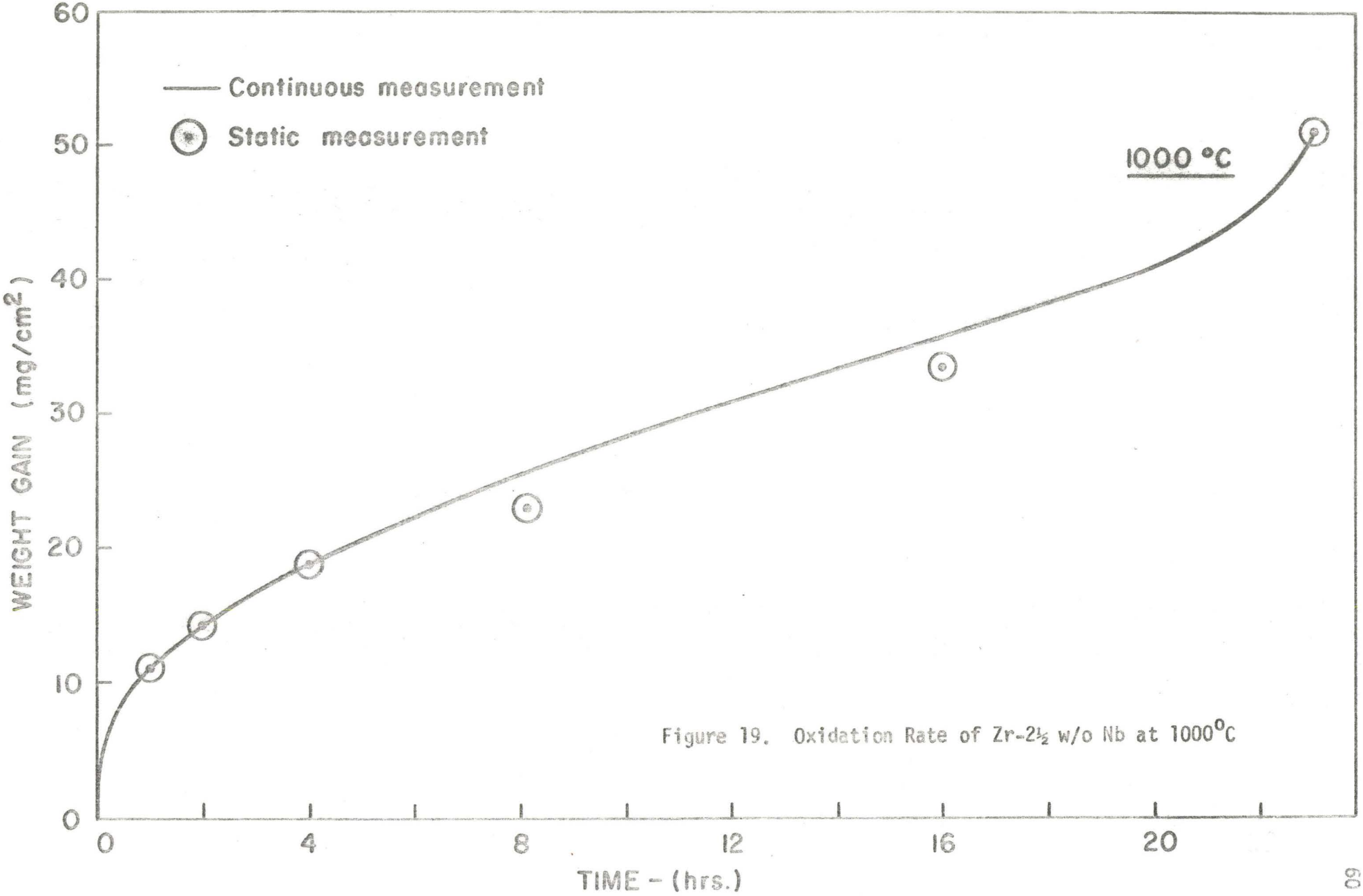

Figure 19. Oxidation Rate of Zr-2½ w/o Nb at 1000°C

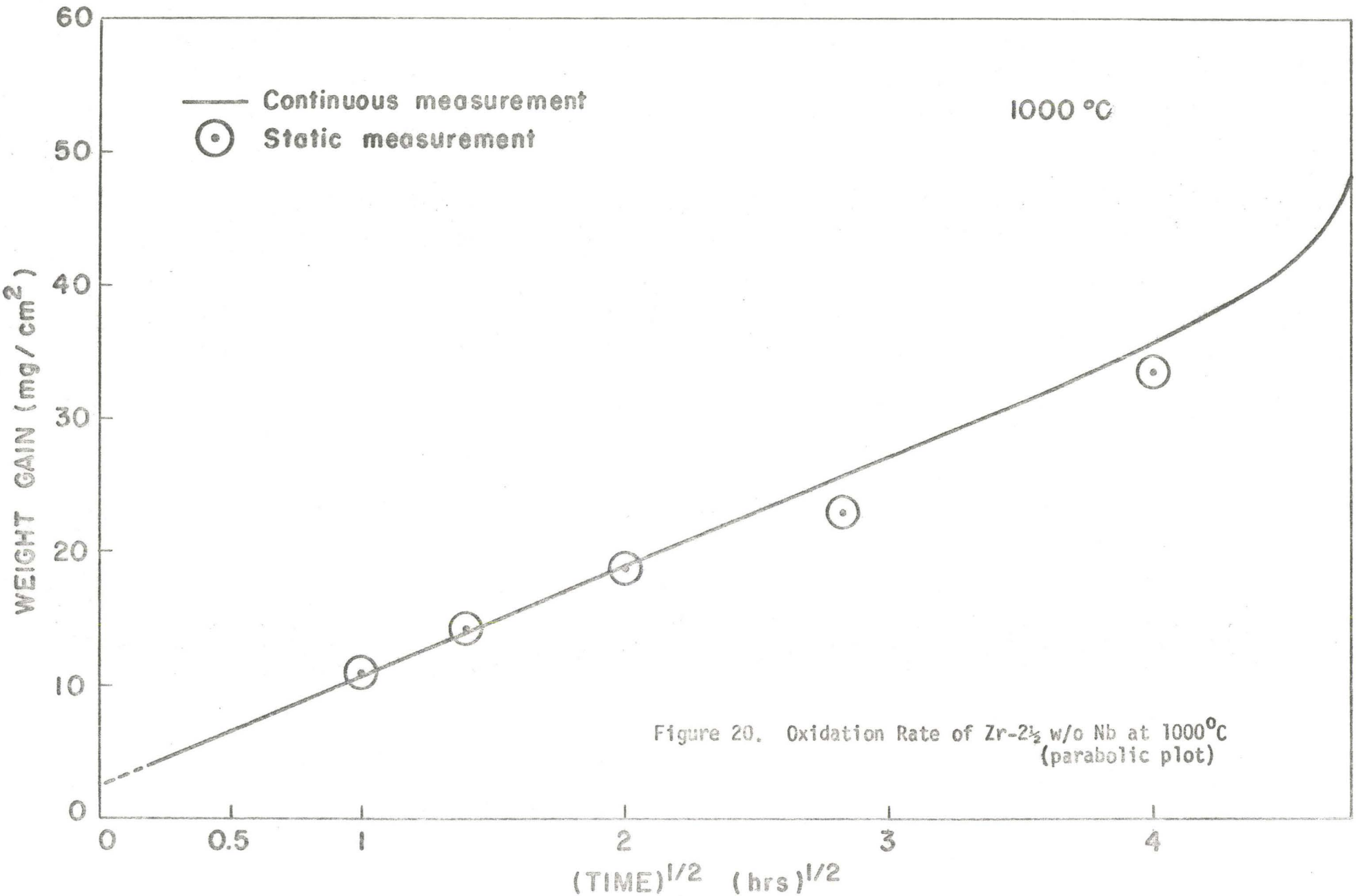

Figure 20. Oxidation Rate of Zr-2½ w/o Nb at 1000°C (parabolic plot)

Specimens oxidized for periods up to 1 hour exhibited a black compact oxide. Those oxidized for longer times were covered with an adherent grey scale. The only white oxide observed was that which formed after breakaway at longer times, the white oxide being concentrated around the region where the breakaway occurred.

5.7 Metallography and Microscopic Observations

The results and metallography in this section are pertinent to measurements and observations at room temperature on the oxide scales and metal substructures formed at the oxidation temperature of 1000°C.

The basic characteristics which a Zr-2½ w/o Nb alloy exhibits during oxidation are an adherent oxide layer growing inwards in contact with a precipitate region which extends into the β-phase of the alloy. Figs. 21 to 23 are a series of micrographs showing the growth of the oxide layer and the metal substructures with varying reaction time. The thickness of the oxide varies from approximately 45 microns at 1 hour to about 105 microns at 8 hours to approximately 220 microns at 23 hours. The growth of the oxide is parabolic up to approximately 12 hours. From the micrographs the oxide appears porous, but the voids arise through polishing and it will be shown later that the oxide is quite compact.

In Fig. 21 we see that underlying the oxide layer there exists a unique columnar structure of α precipitates penetrating from the metal/oxide interface inwards into a martensitic matrix. The martensite matrix is a result of the transformation that occurs when the samples are quenched from the reaction temperature, this temperature being well into the β region.

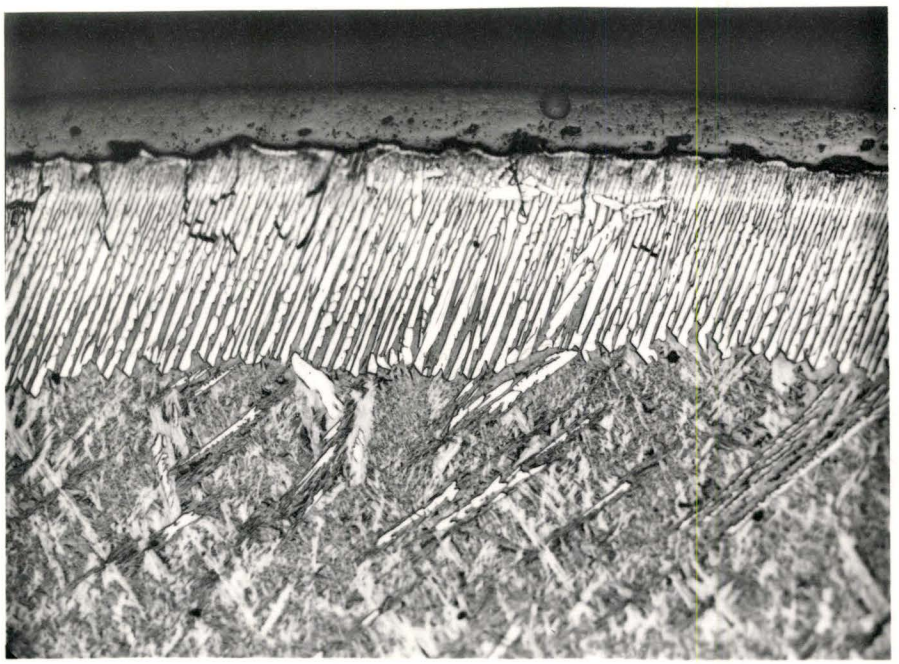

1 hr.

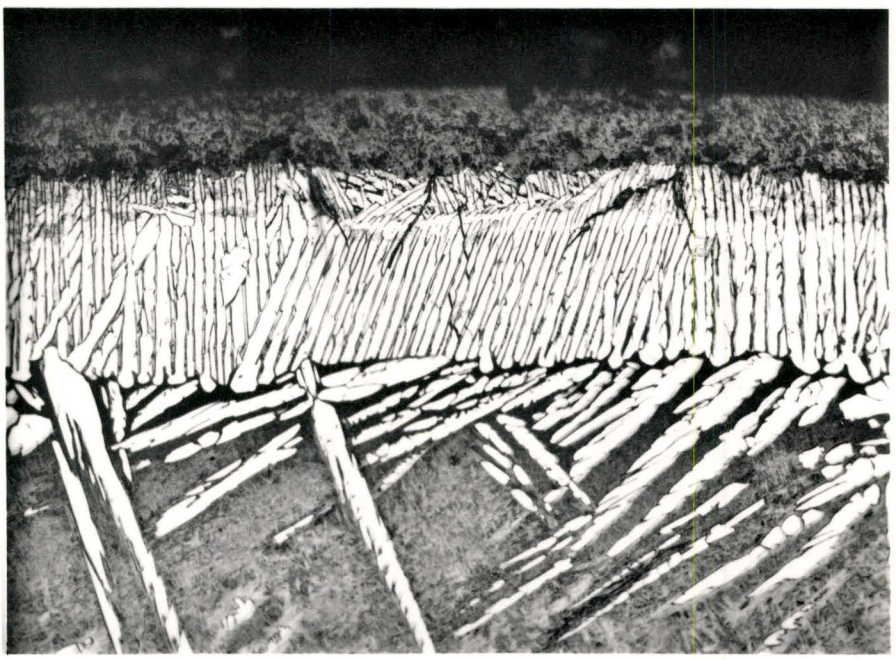

2 hr.

Figure 21. Cross Sections of a Zr-2½ w/o Nb Alloy Oxidized at 1000°C (Magnification 160X)

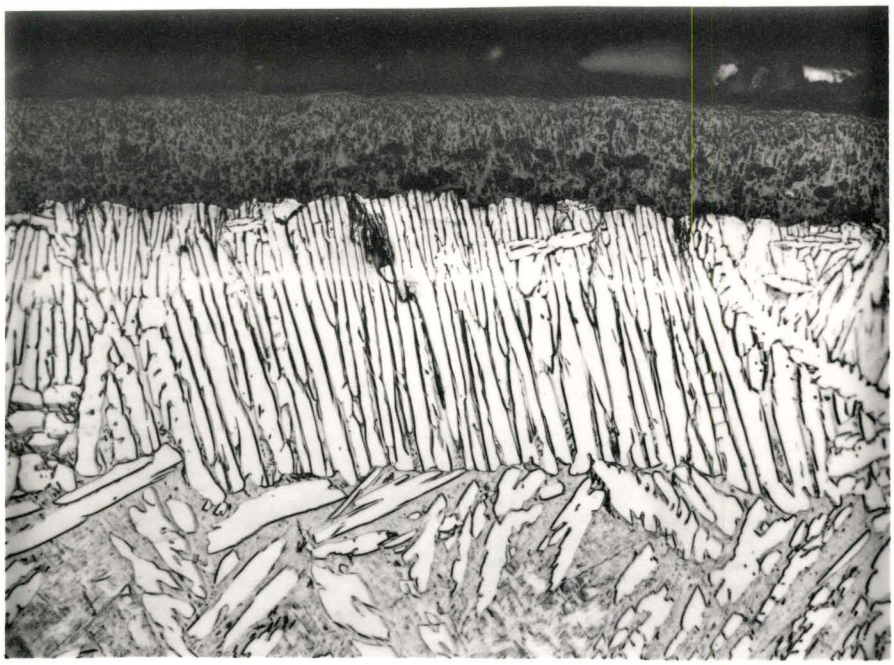

4 hr.

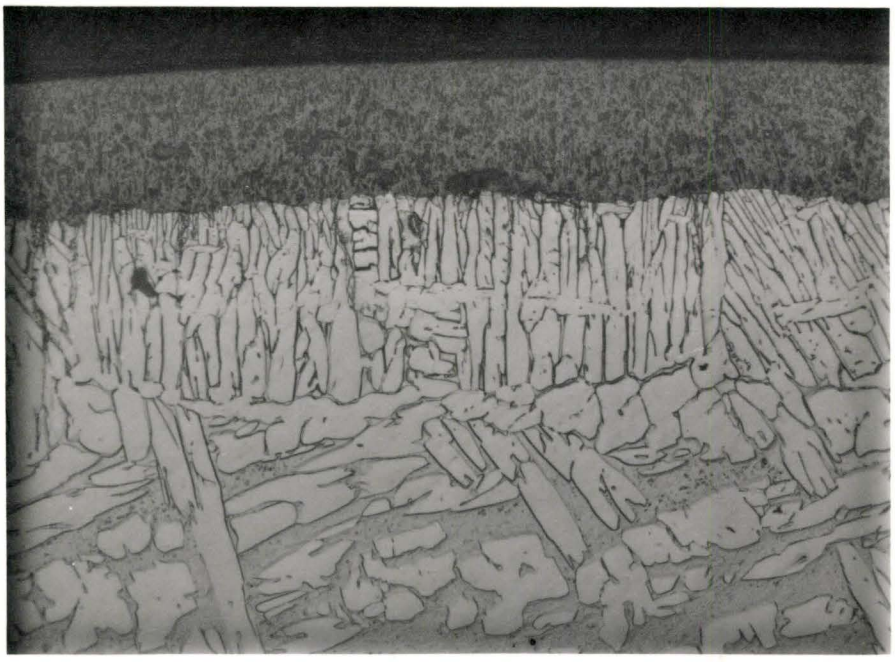

8 hr.

Figure 22. Cross Sections of a Zr-2½ w/o Nb Alloy Oxidized at 1000°C (Magnification 160X)

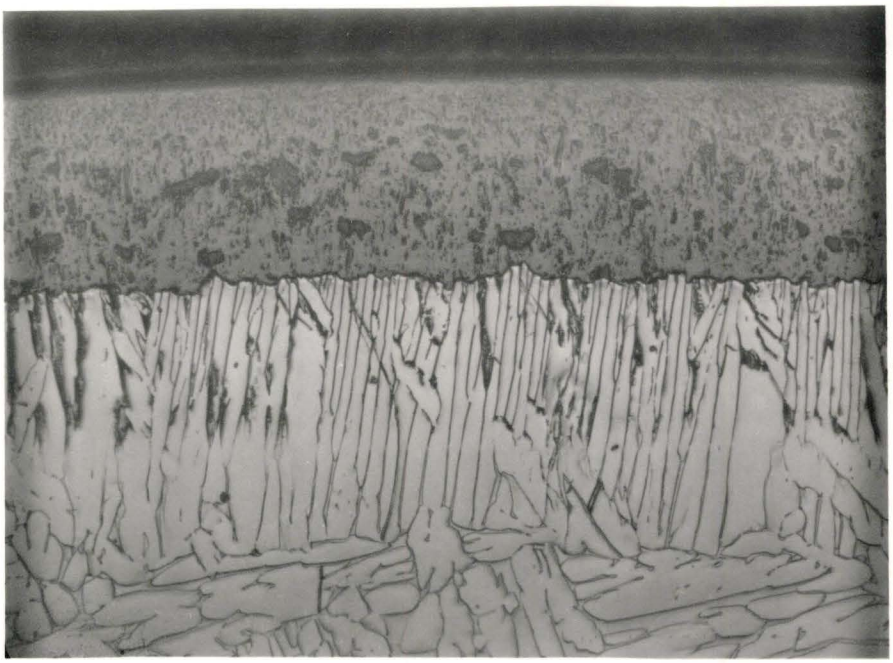

16 hr.

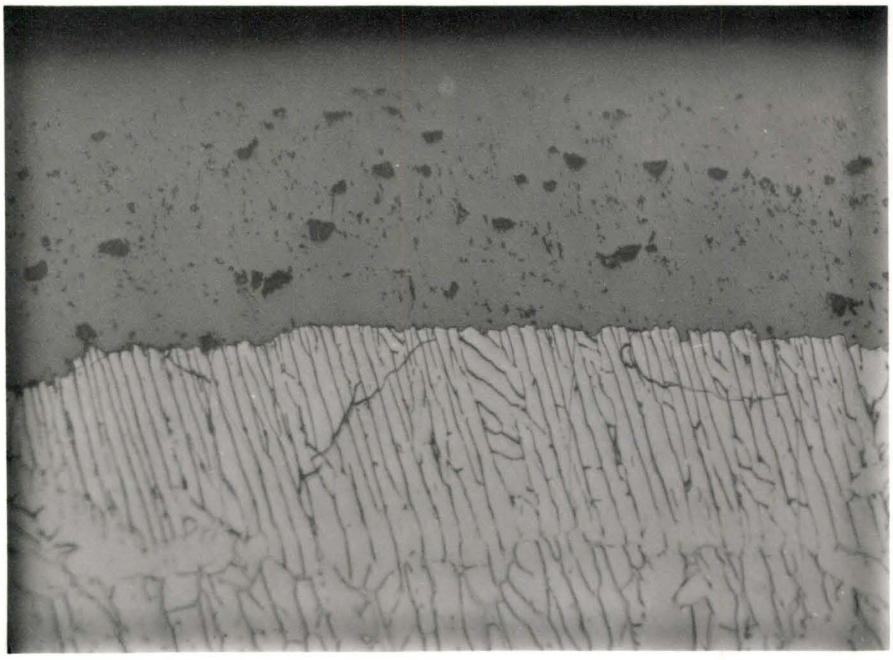

23 hr.

Figure 23. Cross Sections of a Zr-2½ w/o Nb Alloy Oxidized at 1000°C (Magnification 160X)

The precipitates appeared to exist in the form of plates. To verify this a "top view" of this columnar layer was observed by polishing away the overlying oxide layer exposing the precipitate region. By the comparison of this structure as shown in the micrograph of Fig. 24 with those of the normal cross sections from previous micrographs, it should be evident that the precipitates do exist as α-plates. Beneath the region of columnar precipitation there is a region of isolated precipitation as well where isolated plates of the α phase are present in the martensitic matrix. At longer times the columnar layer grows inwards and the precipitates begin to coarsen as shown in Fig. 21 to 23.

Another interesting feature which is evident in Figs. 21 to 23, but, more so in Fig. 25a, is that within the entire columnar region in the underlying metal there exists a region of fine columnar precipitation in the vicinity of the metal/oxide interface. When observed at a higher magnification as in Fig. 25b, it appears that the intercolumnar regions of the coarse and the fine structures differ from one another since they both have different etching characteristics. This is verified by examination of this area using a scanning electron microscope as shown in Fig. 26. The intercolumnar regions of the coarse columnar layer is simply the transformed β phase whereas the material between the columnar precipitates of the fine structure appears to be some form of oxide.

Figs. 27 and 28 are plots of the thicknesses of the alpha + oxide zone versus time and the alpha + beta zone versus time respectively. When the thicknesses are plotted against the square root of time, the straight line which results indicates that the growth of these regions is parabolic.

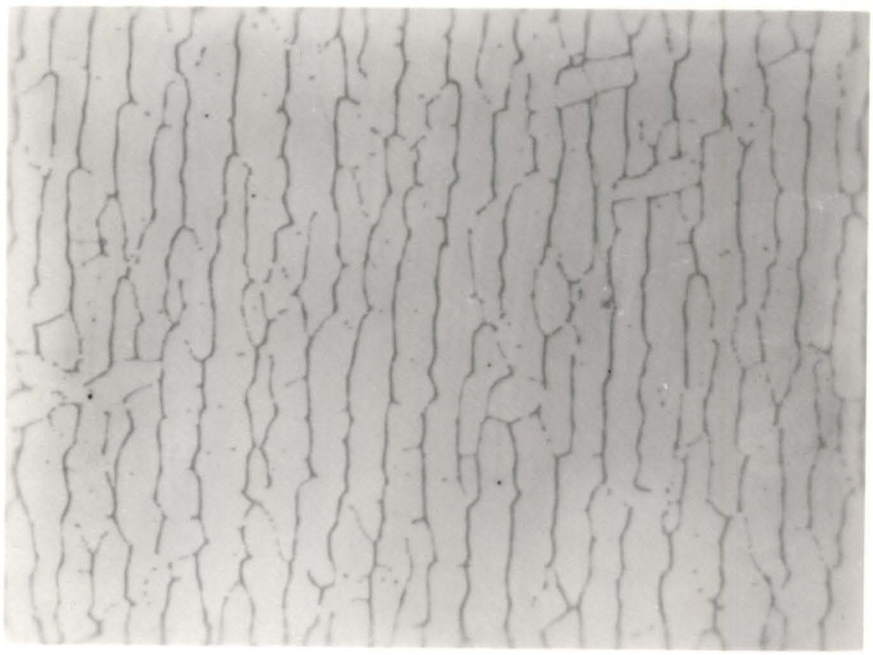

Figure 27. "Top View" of the Columnar Precipitate Region (Magnification 630X)

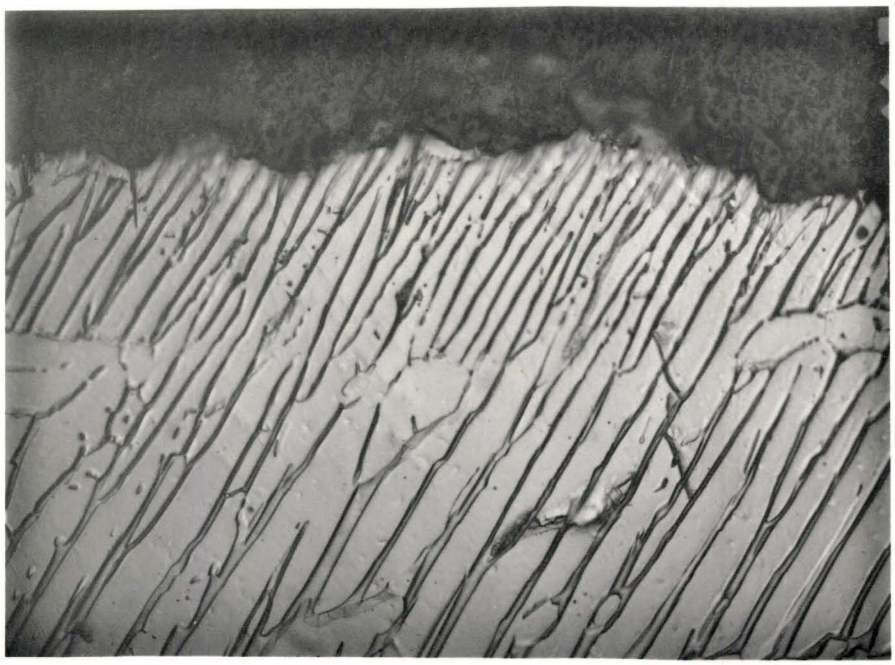

(a) 500X

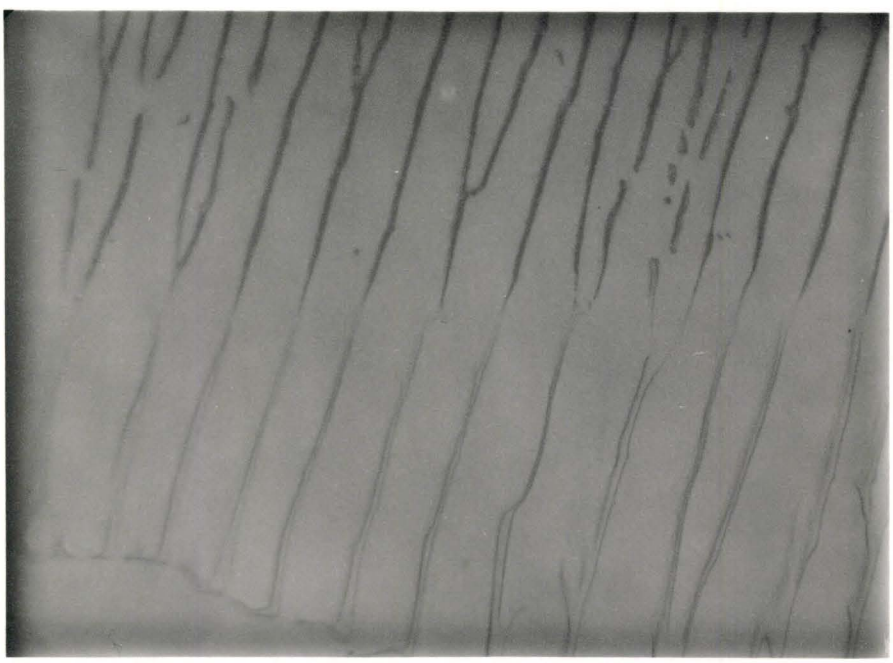

(b) 800X

Figure 25. (a) Micrograph Showing the Fine Columnar Region
(b) Micrograph Showing Differing Intercolumnar Constituents

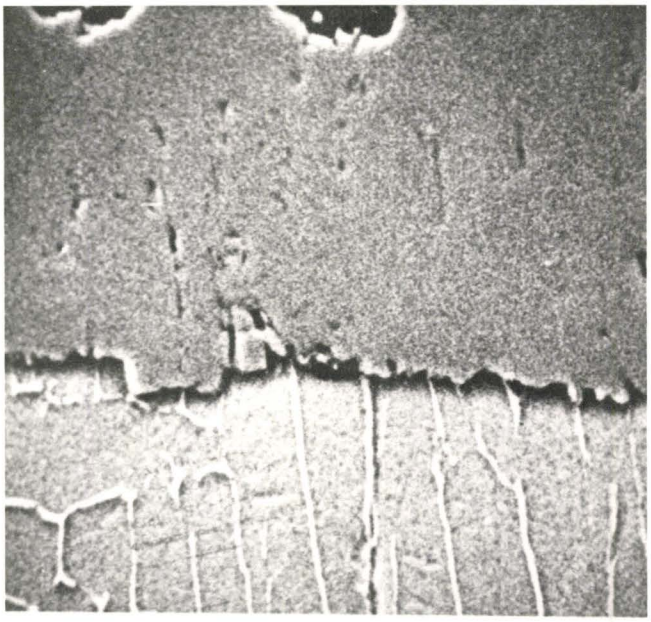

1100X

1100X

Figure 26. Cross Sections of the Internal Oxidation Zone

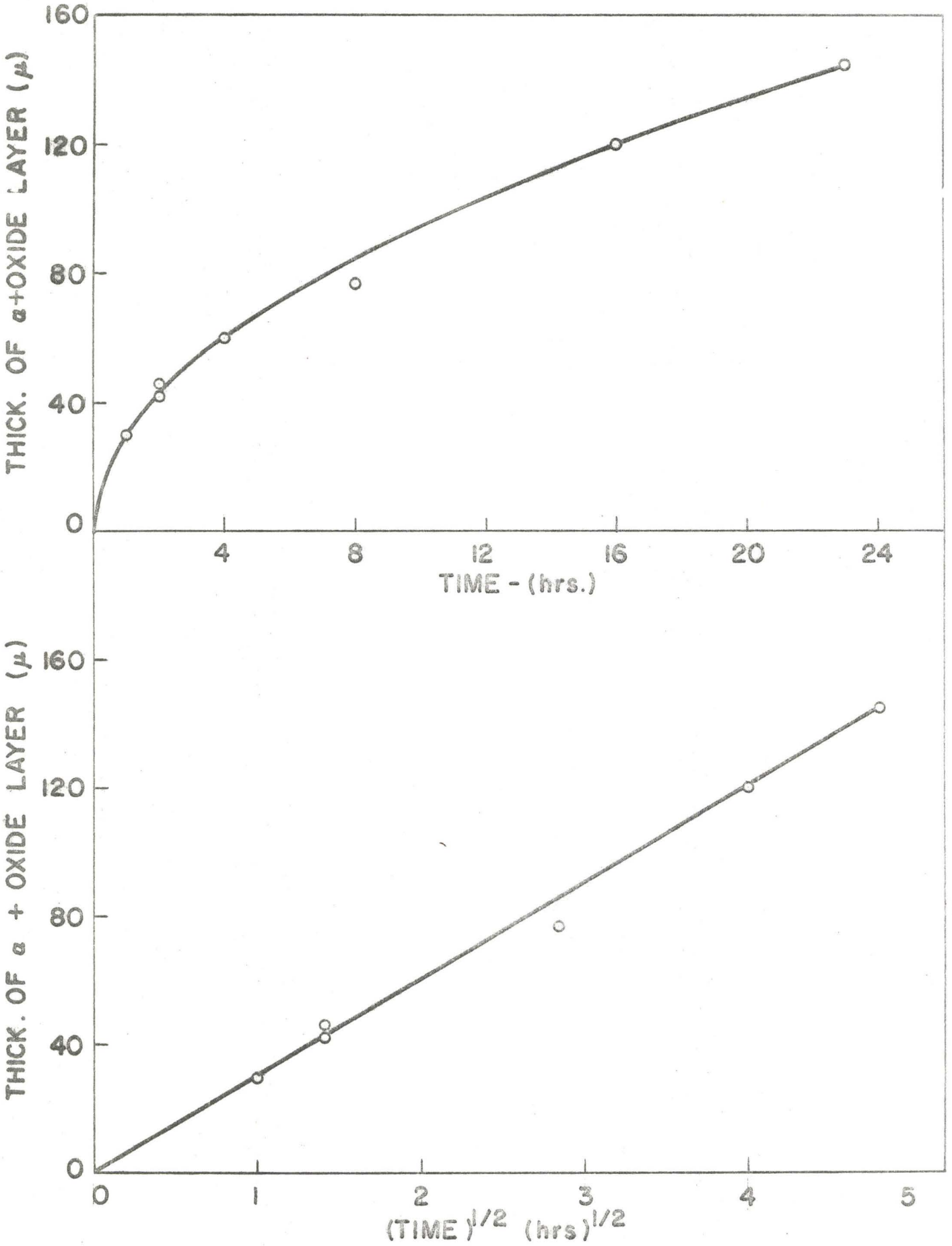

Figure 27. Plot of the Thickness of the α + Oxide Zone versus Time

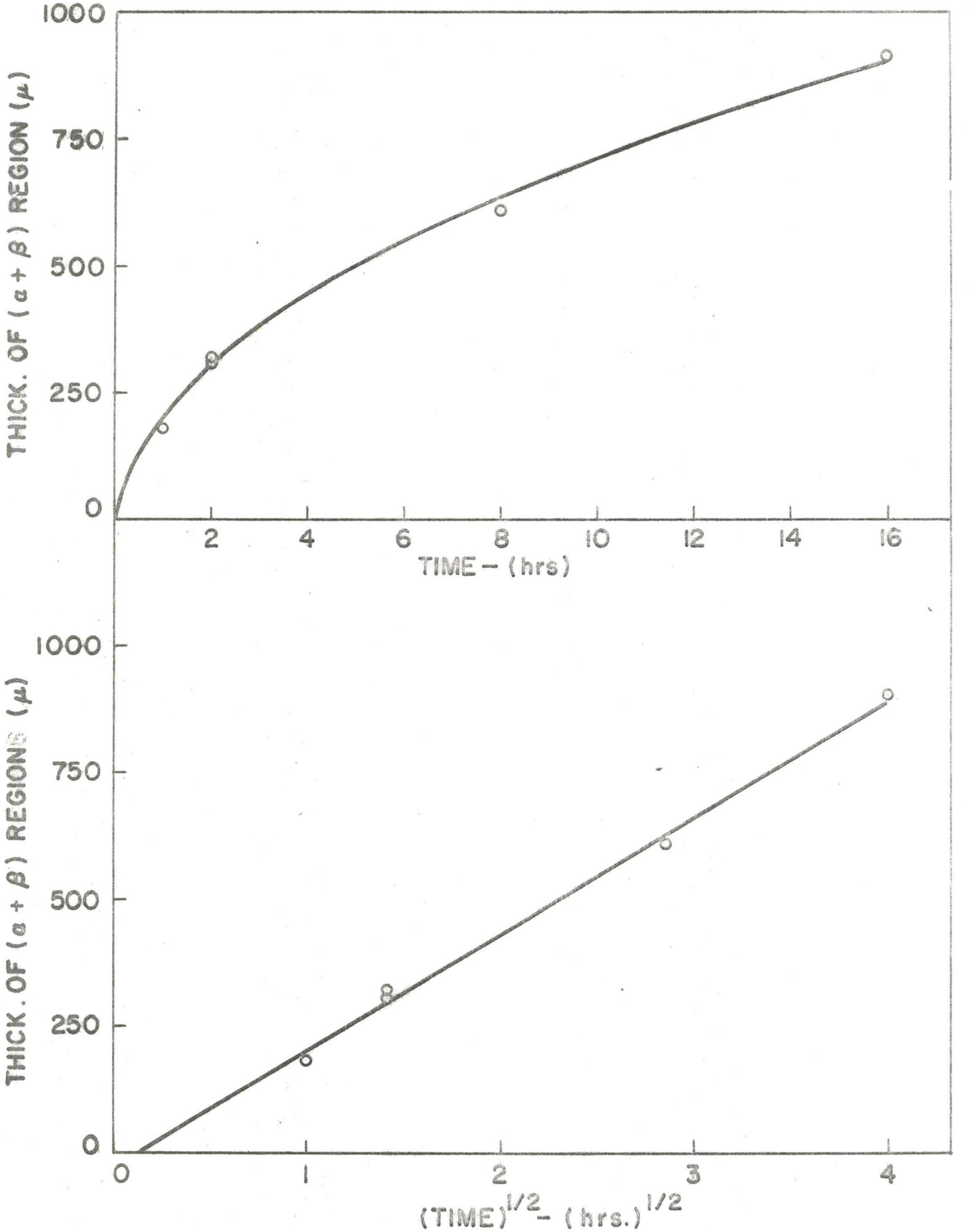

Figure 28. Plot of the Thickness of the α + β Zone versus Time

As pointed out before, the superficial oxide scale does not exhibit a high degree of porosity such as one might be led to believe from earlier micrographs. A more detailed examination of the oxide showed that it exhibited a columnar structure not unlike that of the underlying metal substrate. Also, the columnar grains of the oxide were continuous with the columnar region beneath the scale. The intercolumnar regions of the oxide exhibited an oxide phase(s) different from that of the columnar oxide. The structure of this oxide is shown in Fig. 29 where the columnar grains are clearly evident. A dark intercolumnar oxide appears near the metal/oxide interface extending a short distance into the oxide, whereas farther away from the interface these regions appear lighter.

5.8 Electron Micro-probe Results

The electron micro-probe was used to determine the variations in concentration within the columnar regions of the substructure and oxide. Limitations on the validity of the results were imposed due to the nature of the physical dimensions of the structure. The dimensions were such that the particular area that was being probed was smaller than the electron beam spot and certainly much smaller than the penetration zone of the beam. As a result, the measurements could only be discussed qualitatively due to the nature of the problem.

The structure was scanned both laterally across the columnar structure and in a direction parallel to the α-plates. However, in the latter situation, the results could not even be discussed qualitatively because of the scatter in the counting procedure due to the problem outlined above. The results of the lateral scan showed variations in the niobium content across the

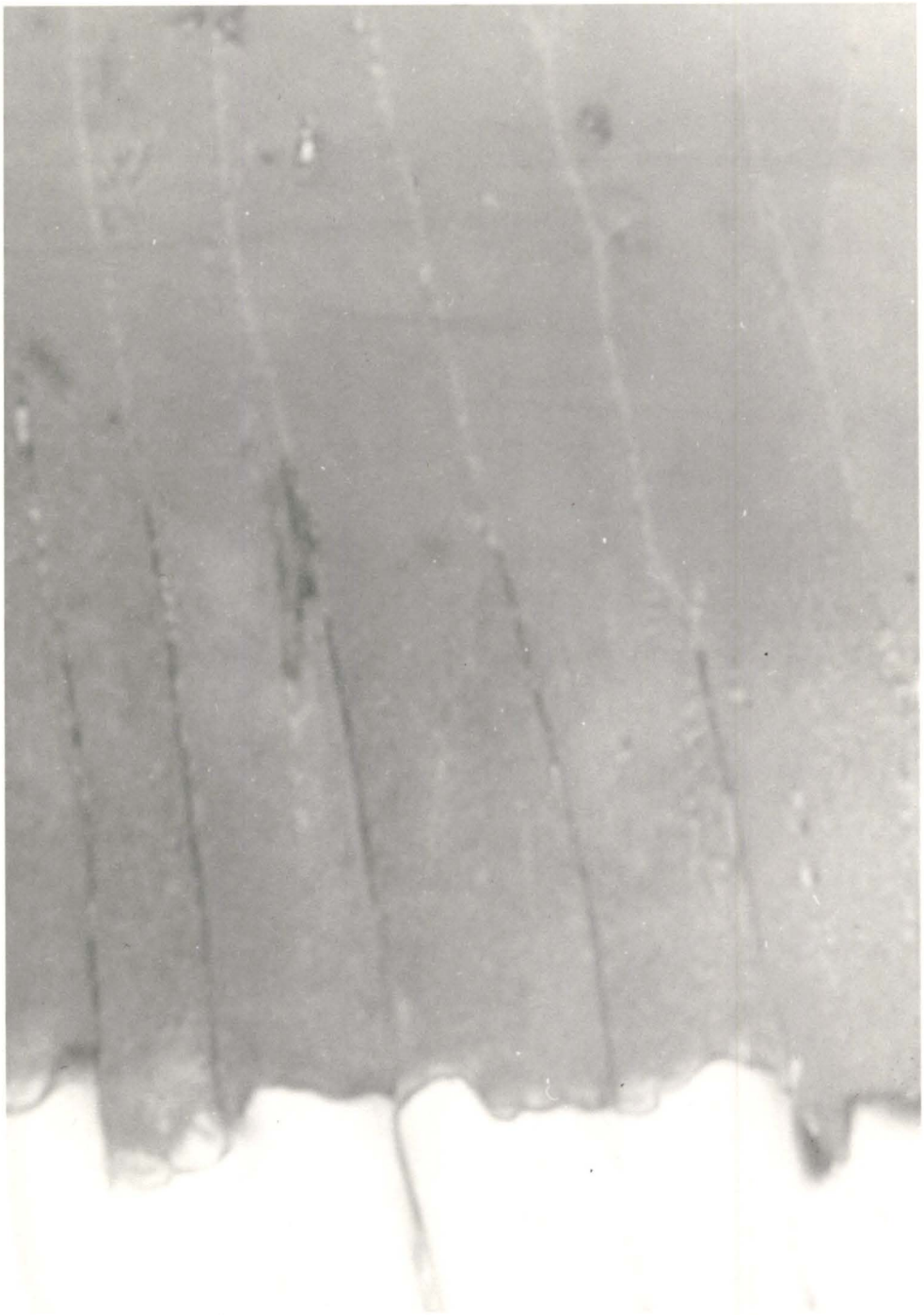

Figure 29. Cross Section of the Multiphase Oxide Scale Near the Alloy/Oxide Interface
(Magnification 4800X)

columnar structure. The peaks in the trace, indicative of a larger concentration of niobium, were generated from areas between the α-precipitates indicating a niobium enrichment in the β-Zr regions. Niobium enrichment in these intercolumnar regions was also observed in the fine columnar region and the oxide as well. A micro-probe trace indicating the niobium segregation is given in the appendix.

CHAPTER VI

Discussion

6.1 Oxidation Rate as a Function of Temperature

The oxidation kinetics of a Zr-2½ w/o Nb alloy is initially parabolic over the temperature range 650 - 1000°C. This suggests that a diffusion mechanism is rate controlling and in particular, the diffusion of oxygen ions via anion vacancies through the scale to the metal/oxide interface determines the reaction rate.

In the high temperature region of the study (937° - 1000°C), the initial parabolic region was followed by a breakaway transition leading to a more rapid reaction kinetics. A brief discussion of some observations associated with the breakaway phenomenon will be presented later. The straight lines of the parabolic plots in the high temperature region do not extrapolate to zero but indicate a weight gain of approximately 1 - 2 mg at the start of the reaction. Rather than being the result of a more rapid reaction rate at the very early stages of oxidation, the occurrence is a result of the experimental technique at the onset of the weight gain determinations. Because zirconium has a very high affinity for oxygen at high temperatures, the specimens acted as an oxygen getter when lowered into the evacuated reaction cell at temperature. During the 15 minute waiting period to ensure the specimens were at the reacting temperature, the specimens picked up residual oxygen from the system which was indicated by a sudden decrease in the pressure of the evacuated chamber as the sample

was lowered in position. Thus at time zero, an initial weight gain would be registered.

In the low temperature region (650°C - 885°C) essentially linear kinetics followed a short region of parabolic behaviour. However, at 650° and 700°C periodic discontinuities in the reaction rate followed the initial parabolic region. Over the entire low temperature range, the near stoichiometric white oxide formed was heavily cracked and the periodic behaviour in the reaction rate is probably a result of the periodic formation and healing of fissures in the scale. Fig. 18b shows the surface of a typical oxide surface formed in this temperature range having large cracks as well as smaller secondary fissures. Bearing in mind that the Pilling-Bedworth's ratio for zirconium metal is of the order of 1.56, it is likely that sufficiently large stresses would exist in the scale such that cracks could be easily initiated.

From the oxidation rate curves, (Fig. 14) it can be seen that the number of discontinuities in the oxidation rate at 700°C is larger than at 650°C over the same period of exposure. At 750°C, a still larger number of these discontinuities is observed but are barely detectable. As their number increases with increasing temperature, they are unable to be detected within the working limits of the assembly. Hence, from 750° - 885°C, the post-parabolic region of oxidation is described by a linear rate even though the discontinuities may exist.

The parabolic rate constants are plotted as a function of temperature in an Arrhenius form, over the entire temperature range investigated (Fig. 30). Two straight line relationships result with the discontinuity occuring between 885°C and 937°C. In the high temperature region (937° - 991°C), K_p as a

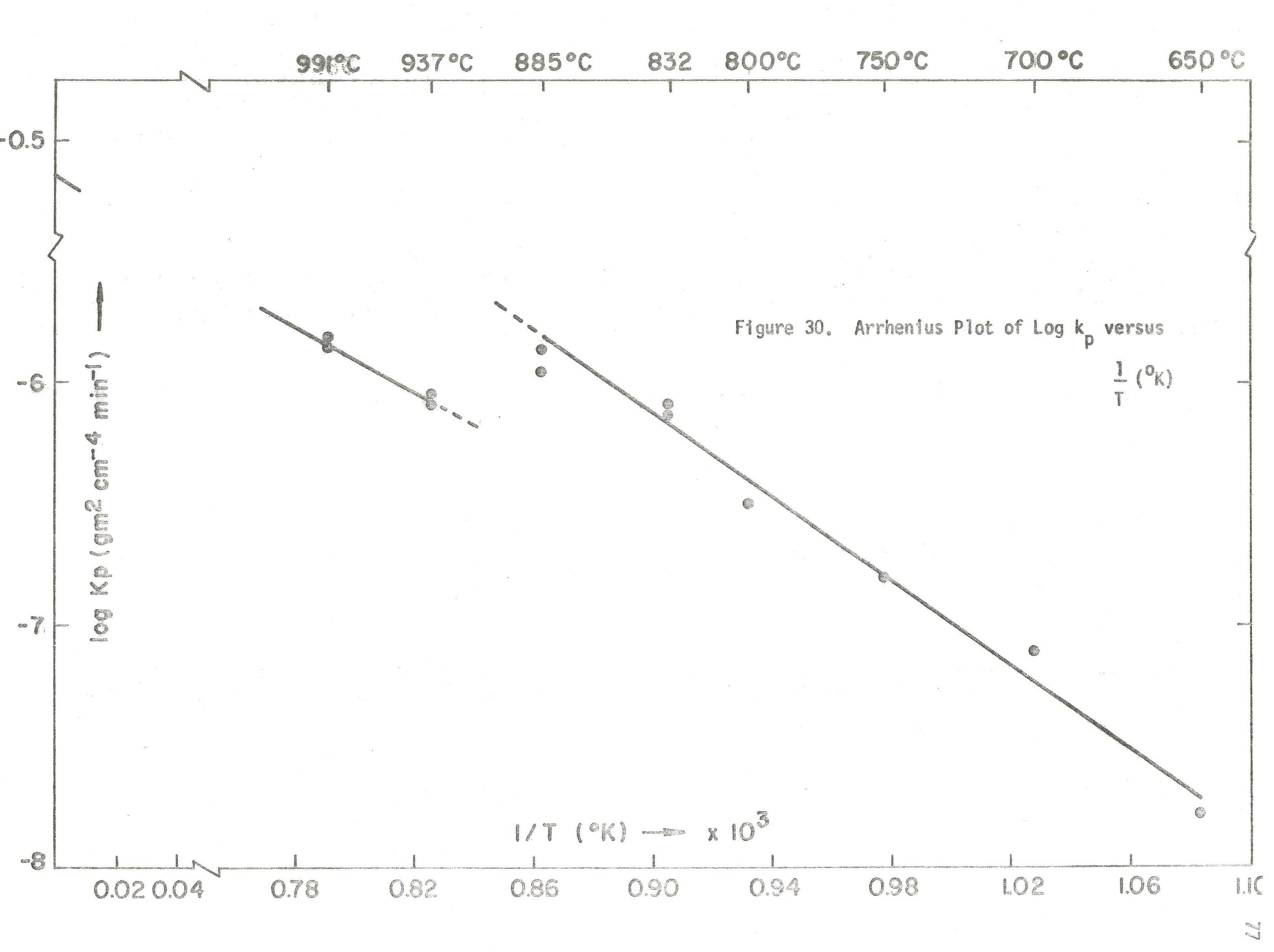

Figure 30. Arrhenius Plot of Log k_p versus $\frac{1}{T}$ (°K)

function of temperature can be described by the following expression:

$$K_p = 0.22 \exp\left(\frac{-30054}{RT}\right) \qquad (6\text{-}1)$$

where $E_{act} \simeq 30$ kcal/mole.

In the low temperature region (650° - 885°C), K_p as a function of temperature can be described by the following expression:

$$K_p = 20.9 \exp\left(\frac{-38026}{RT}\right) \qquad (6\text{-}2)$$

where $E_{act} \simeq 38$ kcal/mole.

The discontinuity observed in the Arrhenius plot is attributed to the $\beta/\alpha + \beta$ phase boundary of the Zr-Nb phase diagram. From the phase diagram (Fig. 5), the $\beta/\alpha + \beta$ transition for a Zr-2½ w/o Nb alloy occurs at about 840°C, and one would expect the discontinuity in the oxidation rates to occur around this temperature rather than in the observed temperature range of 885° - 937°C. It must be remembered that the binary phase diagram is constructed on the basis that the alloy phases contain virtually no oxygen whatsoever and the solid line describing the $\beta/\alpha + \beta$ phase boundary in Fig. 5 is constructed on this basis. However, Winton and Murgatroyd[50] have shown that the influence of an impurity such as oxygen in Zr-Nb alloys results in a shift of the $\beta/\alpha + \beta$ phase boundary. In particular, the dotted line in Fig. 5 represents the $\beta/\alpha + \beta$ phase boundary for Zr-Nb alloys containing about 1400 ppm O_2. They have concluded that a Zr-2½ w/o Nb alloy with the above oxygen content is only fully in the β-phase above approximately 925°C. The oxygen content of the samples used in this investigation after the annealing treatment was approximately 1000 ppm. Thus the conclusion that the observed discontinuity is a result of the $\beta/\alpha + \beta$ phase boundary

is justifiable when consideration is made with respect to the position of the $\beta/\alpha + \beta$ phase boundary due to the residual oxygen content of the alloy.

6.2 X-ray Analyses

In the high temperature range, two forms of oxide were observed. X-ray powder patterns of both the grey and the white oxides revealed virtually no differences in crystal structure between the two forms. The colour differences between the two oxides are due to changes in stoichiometry, the white form being near stoichiometric. X-ray diffractometer measurements provided a more detailed method for identification purposes. The main reaction product was identified as monoclinic zirconia (ZrO_2). The extra reflection at a d-spacing of 2.97 Å was attributed to the presence of the mixed oxide, $6ZrO_2 \cdot Nb_2O_5$ which has a strong reflection at 2.95 Å. It is believed that the extra diffraction peak is also a result of the mixed oxide rather than tetragonal zirconia because certain observed peaks corresponding to the monoclinic structure had larger intensity ratios (I/I_o) than expected; these particular peaks (see Table II) correspond to the more intense reflections of the mixed oxide, $6ZrO_2 \cdot Nb_2O_5$. The presence of $6ZrO_2 \cdot Nb_2O_5$ in oxides formed on Zr-Nb alloys at high temperatures has also been confirmed by Zmeskal and Brey[43] and Guerlet and Lehr[48].

Examination of the oxide at the metal/oxide interface revealed that only monoclinic ZrO_2 is present. The observed intensity ratios do not all correspond to those given in the A.S.T.M. powder data file (see Table III); however, this can be expected since the specimen was a solid oxide scale rather than a powdered form, and the effect of preferred orientations would alter the intensity ratios. The absence of the extra reflection corresponding

to the mixed oxide indicates that the latter is present in the oxide but not in the vicinity of the metal/oxide interface. Thus in the oxide adjacent to the metal/oxide interface only monoclinic ZrO_2 is present whereas away from the interface both monoclinic ZrO_2 and the mixed oxide $6ZrO_2 \cdot Nb_2O_5$ exist.

6.3 Oxidation of a Zr-2½ w/o Nb Alloy at 1000°C

Oxidation of alloy spheres resulted in the extension of the period of parabolic behaviour up to approximately 12 hours due to the minimization of the edge effect which is characteristic of rectangular plate samples. The slight reduction in the value of K_p for the spherical specimens is attributed to the non-existing edge effect.

At short times (1 hour) a black adherent oxide was formed which progressively transformed to a compact pearly grey oxide at longer times. The white form of ZrO_2 was only observed on specimens in the breakaway region and was concentrated around the region where breakaway occurred. As pointed out before, the colour changes are associated with changes in stoichiometry.

The cross-sections of the oxidized samples are characterized by:

(i) a compact scale exhibiting a columnar morphology containing more than one oxide and showing deviations in stoichiometry,

(ii) a zone of internal oxidation comprised of the α-Zr phase plus an oxide,

(iii) a zone of internal precipitation where the α-Zr phase is precipitated in a matrix β-Zr resulting in a columnar-plus-isolated-precipitate two-phase zone,

(iv) and a region of transformed β-Zr extending to the interior of the sample.

An idealized schematic representation of the above description resulting from metallographic observations is shown in Fig. 31b. Fig. 31a is the Zr rich position of the Zr-Nb-O ternary isotherm at 1500°C as constructed by Wyder and Hoch[51]. (The tie lines in the two-phase regions have been drawn by the author for illustrative purposes only and are not a result of actual determinations.) Since a ternary isotherm at 1000°C was not available in the literature, the isotherm of Wyder and Hoch will be used to qualitatively discuss the observed microstructures, assuming that the two isotherms are relatively similar, differing only in slight compositional changes of the respective phases. This assumption appears to be valid since the phases across the respective binary phase diagrams at 1000°C coincide with the binary representation on the ternary phase diagram at 1500°C.

The identity, order and structure of ternary diffusion layers have been studied in diffusion couples and the sequence of layers always corresponds to consecutive regions in the appropriate ternary isotherm of the phase diagram. Using diffusion layer formation in the Al-Mg-Zn system, Clark and Rhines[52] proposed a set of rules governing the course of the composition path in multi-layered ternary diffusion structures which was later modified by Kirkaldy and Brown[53], supported by observations in the Cu-Zn-Sn system. In simple binary diffusion couples only single phases are present since the phase rule defines a unique composition path corresponding to a tie-line in two-phase fields. In ternary systems, because of the extra degree of freedom, the composition path may cross tie lines in two-phase

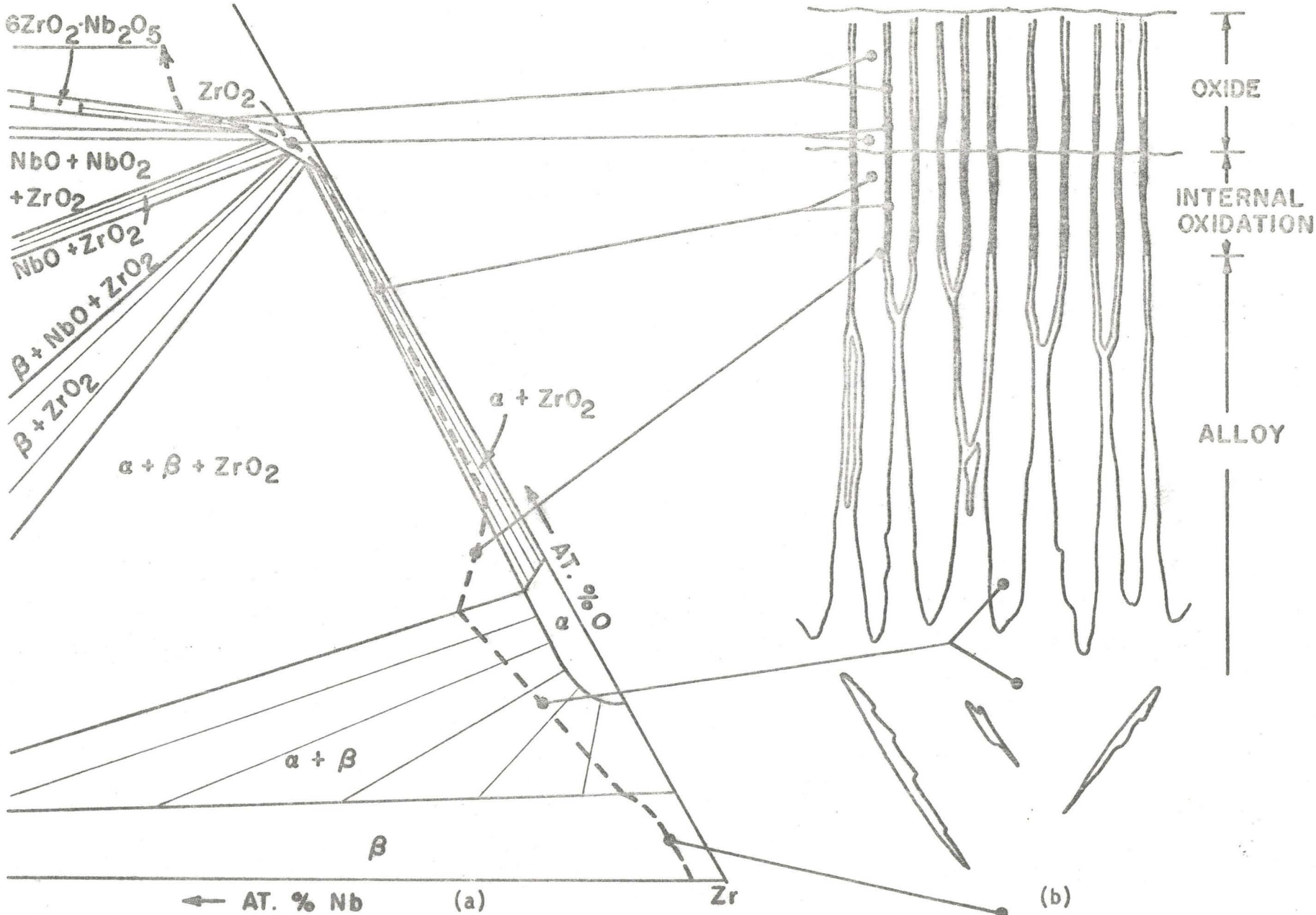

Figure 31. Schematic Representation of the Cross Section and the Composition Path Defining the Observed Structures

fields resulting in a diffusion layer having two phases.

A composition path can be qualitatively constructed on the isotherm of the ternary phase diagram to account for the observed microstructure of the oxidized alloy. We essentially have a diffusion couple consisting of pure oxygen and a Zr-2½ w/o Nb alloy. The terminal points of the composition path are thus defined by these compositions and the resulting phases, after oxidation, can be described by the consecutive regions which are traversed by a path having the above terminal compositions. Fig. 31a shows the composition path constructed on the ternary phase diagram and how the successive regions along the path correspond to the observed microstructure.

The composition path emerging into the β region from the Zr-Nb side of the ternary defines the presence of the β phase at the interior of the specimens. Upon emergence into the two-phase α + β region, the crossing of tie-lines results in the precipitation of α-Zr producing a two-phase α + β layer. The zone of internal oxidation consists of α-Zr and an oxide. The only oxide which can exist in equilibrium with α-Zr is ZrO_2. For the composition path to continue through the two-phase α + ZrO_2 region of the phase diagram, it must do so by crossing the three phase α + β + ZrO_2 region upon emergence from the α + β region. Cutting through the three phase field defines the interface between the α + β and the α + ZrO_2 layers where the three phases, α + β + ZrO_2, are in equilibrium. The three phase equilibria is supported by metallographic observations in Fig. 26. For the formation of ZrO_2 as an internal oxidation product, the composition path crosses tie lines in the two-phase α + ZrO_2 region before entering the ZrO_2 phase field. The ZrO_2 layer, adjacent to the zone of internal oxidation, metallographically appears as if it were a two-phase zone. Since X-ray

examinations of the underside of the scale revealed only the presence of monoclinic zirconia with no reflections corresponding to the mixed oxide or lower oxides of niobium, it is believed that the dark constituent of this layer corresponds to ZrO_2 with Nb dissolved in it thus altering the stoichiometry. Electron micro-probe analysis of the dark constituent revealed a Nb enrichment in these regions and the sequence of events leading to the formation of the oxide explains the observed enrichment. In the $\alpha + \beta$ region near the $\alpha + \beta/\alpha + ZrO_2$ interface, the β phase is enriched in Nb due to Nb rejection from α-Zr as the latter is precipitated. It is these Nb enriched β regions which subsequently oxidize internally to form ZrO_2 with Nb dissolved in it. These dark stringers of Nb enriched zirconia extend continuously across the alloy/oxide interface into the adjacent oxide layer. Hence the two-phase appearance of the ZrO_2 layer is due to the Nb segregation in the oxide which consequently influences the stoichiometry; the presence of the ZrO_2 layer coincides with the composition path cutting through the ZrO_2 phase field.

Emergence of the diffusion path into the two phase field of $ZrO_2 + 6ZrO_2 \cdot Nb_2O_5$ at an angle incident to the tie-lines results in a two phase layer consisting of zirconia and the mixed oxide. The thickness of the two phase layer is approximately 6/7 that of the entire oxide; the remaining 1/7 corresponds to the zirconia layer. The presence of the mixed oxide has been confirmed by X-ray diffraction.

The two-phase region of the oxide, above the zirconia layer, does not extend to the surface of the oxide as shown in the schematic. This can be expected because of the fact that for the two-phase columnar structure to exist in the oxide, it is necessary that the alpha structure be stabilized

beneath the oxide scale. Since the oxide grows by the inward diffusion of oxygen, the initial oxide which is formed is that which exists at the surface of the scale. At the initial stages of oxidation the alpha structure is not yet stabilized as a columnar structure and thus the oxide formed initially would not have this characteristic morphology, and, as a result, appears as a thin homogeneous region of ZrO_2.

It is evident from Figs. 21 to 23 and Fig. 25a that the zone of internal oxidation has a finer structure than the coarse $\alpha + \beta$ region beneath it. With the alloy/internal oxidation interface parabolically advancing inwards and the coarse α plates acting essentially as markers, one would expect the zone of internal oxidation to have a coarse columnar structure not unlike that of the $\alpha + \beta$ region. However, the fine structure observed in the $\alpha + ZrO_2$ layer is a result of the nucleation of secondary α plates in the β phase between the existing coarse α plates. The nucleation and growth of these new plates in the $\alpha + \beta$ region ahead of the advancing internal oxidation front results in a finer structure of the latter. Metallographic evidence of this secondary nucleation of α-plates is shown in Fig. 32.

When α-plates are initially stabilized beneath the oxide scale, certain plates will tend to grow faster than others resulting in a fine structure in the internal oxidation zone while the $\alpha + \beta$ region would appear coarse. The faster growing plates would retard the growth of the slower ones by eventually growing around them. Thus the fine structure of the internally oxidized layer would only be evident at short times while at longer times, the advancement of the $\alpha + \beta + ZrO_2$ interface across the

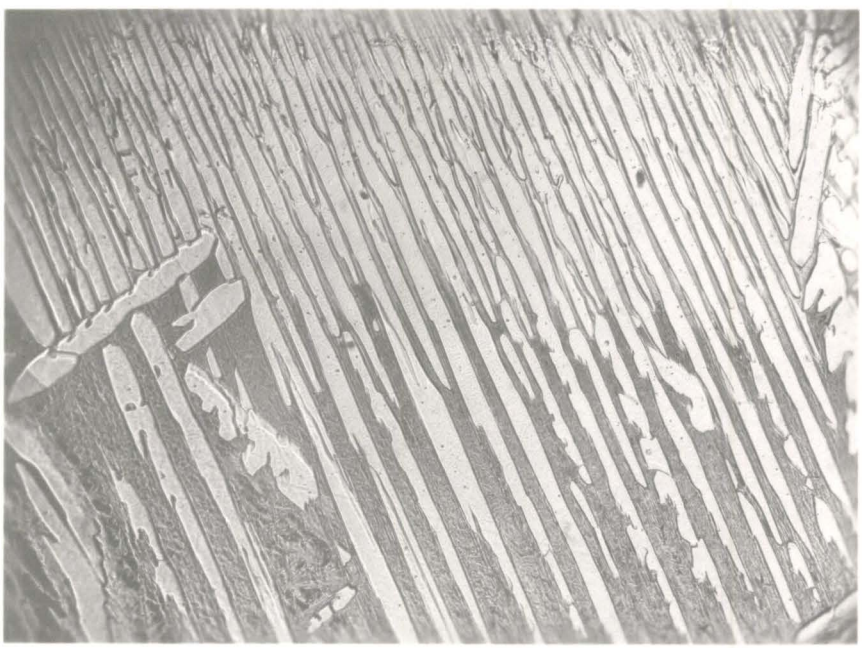

1 hr. at 1000°C

Figure 32. Cross Section Showing Secondary Nucleation of α Plates in the α + β Precipitate Region (Magnification 400X)

coarse $\alpha + \beta$ region would result in a coarse $\alpha + ZrO_2$ region as well. However, as pointed out before, the existence of a fine structured $\alpha + ZrO_2$ layer over all times can be attributed to the nucleation of new α-plates. The nucleation of new plates between the existing columnar α structure can be justified by the slope of the $\beta/\alpha + \beta$ phase boundary of the Zr-Nb-O isotherm. From the phase diagram it is apparent that the oxygen solubility in the β phase decreases with increasing Nb concentration. As the α-Zr plates are growing, Nb is being segregated into the intercolumnar regions of β-Zr, thus decreasing the oxygen solubility. As a result, areas of oxygen supersaturation are created, the supersaturation being relieved by the nucleation and growth of secondary α-plates. Hence the fine structure of the $\alpha + ZrO_2$ diffusion layer is maintained at longer times by continued nucleation and growth of new plates relieving the supersaturated conditions which are created in the coarse columnar region as the $\alpha + \beta + ZrO_2$ interface advances inwards; this is shown schematically in Fig. 31b.

Internal oxidation in the Zr-Nb system has been observed by Rapp and Goldberg[45] in Nb-Zr alloys, up to 40 a/o Zr, oxidized at 1000°C in oxygen. Alpha zirconium, stabilized ahead of the advancing internal oxidation zone, was oxidized internally to ZrO_2. In a recent investigation by Guerlet and Lehr[48], to which reference has already been made, the columnar alpha structure was observed beneath a columnar oxide scale, not unlike that observed in this investigation. However, there was no evidence that an internal oxidation zone was formed nor did they observe any variations in the colour of the oxide in the intercolumnar regions of the scale. While no micrographs of the metal/oxide interface at high magnifications was

presented by Guerlet and Lehr, it was from metallographic evidence such as this that the presence of these zones was confirmed in this work.

Guerlet and Lehr argued that the intercolumnar regions of the metal near the metal/oxide interface was primarily β-Nb and that α-Zr and β-Nb oxidized simultaneously to form ZrO_2 and Nb_2O_5 respectively, while a solid-solid reaction taking place between the latter to form $6ZrO_2 \cdot Nb_2O_5$ accounted for the mixed oxide reflection in the X-ray results. Because of the difficulty in assessing the micro-probe data for the intercolumnar regions of the metal near the interface, due to the size limitations of the system, the author is unable to accept the conclusion that these areas are β-Nb but can accept the fact that there is niobium enrichment in a β-Zr phase. It is believed that the enriched β-Zr phase oxidizes to form the dark stringers of ZrO_2 enriched in Nb, which will be designated as ZrO_2(Nb). It is the ZrO_2(Nb) which oxidizes to $6ZrO_2 \cdot Nb_2O_5$ when a sufficient oxygen level is attained in the scale. This reaction is represented by the conversion of the dark ZrO_2(Nb) in the zirconia layer to the white $6ZrO_2 \cdot Nb_2O_5$ in the two-phase oxide layer.

It is believed that the protective qualities of the grey oxide scale can be attributed to the structural nature of the internal oxide precipitates. The fact that the oxide stringers of ZrO_2(Nb) extend continuously from the zone of internal oxidation across the metal/oxide interface into the oxide scale, may account for the exceptional adherence which the oxide displays, in the region of parabolic behaviour.

6.4 Breakaway Oxidation

Breakaway oxidation is a very complex phenomenon that is not well

understood. It has been previously pointed out that certain factors such as changes in stoichiometry, crystallographic changes or induced stresses in the oxide as a result of volume changes may promote fractures leading to the breakaway phenomenon. It is not the purpose of this section to propose a mechanism to explain breakaway but to discuss some of the observations related to it.

Breakaway to a more rapid reaction kinetics was most pronounced in the high temperature range. Stoichiometric white ZrO_2 appearing along the edges of rectangular samples and a white network superimposed on the compact grey ZrO_2 of the surfaces are characteristic of a Zr-2½ w/o Nb rectangular specimen oxidized in the breakaway region at high temperatures[47]. Using the spherical samples, breakaway was characterized by rapid attack at localized areas resulting in the formation of the white stoichiometric ZrO_2 at these points. A cross section of a region of localized attack resulting in breakaway kinetics is shown in Fig. 33b. The oxide overlying the columnar structure is the compact grey ZrO_2 while the cracked and massive scale growth above the cavity produced at the metal surface is the white stoichiometric ZrO_2. The interesting feature associated with this localized attack is the difference in alloy microstructure beneath the respective oxides. At the metal/oxide interface bordering the cavity, the columnar structure has broken down and a more rapid attack is tolerated in this region whereas a compact grey adherent scale exists only in those areas where the columnar structure is maintained.

Since the Pilling-Bedworth ratio for zirconia/alpha-zirconium is larger than unity (~1.56) large stresses may be generated in the oxide. As a result, fissures in the oxide may be initiated by shearing, a process

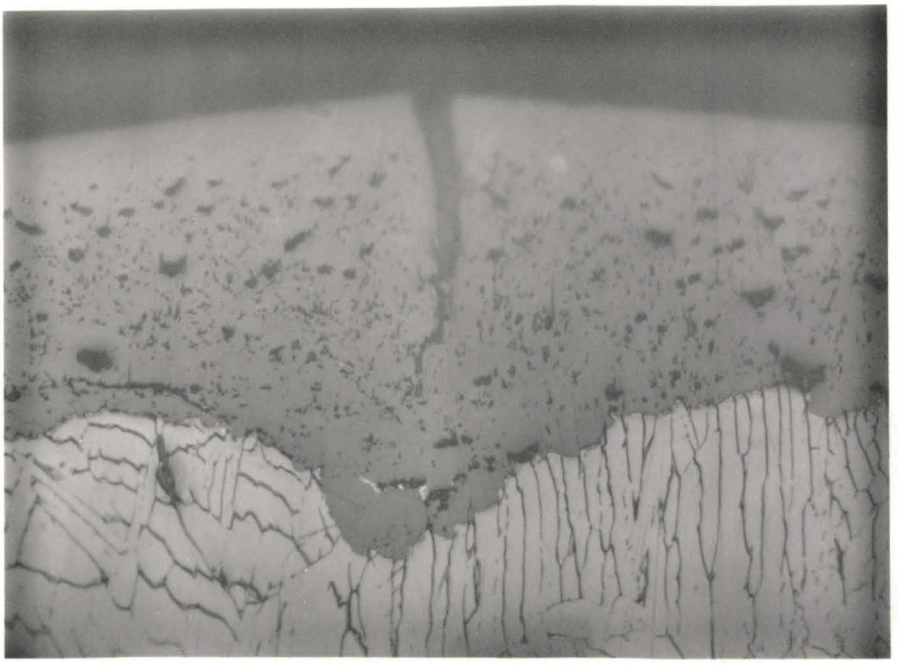

(a) 160X

(b) 80X

Figure 33. (a) Initiation of Localized Attack
(b) Cross Section of a Region of Localized Attack (Breakaway)

which would be favourable in this system due to the columnar morphology which the oxide exhibits. Cracks such as shown in Fig. 33a may be generated from small fissures under the influence of stresses in the oxide resulting in the initiation of localized attack. Once the crack propagates to the metal interface, oxygen supply would come in direct contact with the metal and the oxidation reaction would become catastrophic. As a result, this may lead to the situation shown in Fig. 33b where the columnar structure has been consumed and the protective qualities have been lost. Since the oxidation rate is very rapid in the region of localized attack, almost all of the oxygen may be consumed in forming the oxide leaving an insufficient amount available to stabilize the columnar structure; that is to say, that due to the cracked and porous nature of the scale in the breakaway zone, the reaction may occur to such a rapid extent, that the metal/oxide interface may advance at a faster rate than the rate at which α-Zr may be stabilized ahead of the moving front. Under these conditions, rapid reaction kinetics would persist until all of the metal was consumed.

CHAPTER VII

Conclusions

(i) The oxidation of a Zr-2½ w/o Nb alloy initially obeys a parabolic relationship over the range 650° - 1000°C. Parabolic behaviour was followed by a transition to a more rapid reaction kinetics. In the range 650° - 885°C, the parabolic region extends over relatively brief time periods as compared to the high temperature range (937° - 1000°C). The activation energy for parabolic oxidation from 650° - 885°C is 38 kcal/mole. Oxidation in the low temperature range is characterized by a transition to essentially linear kinetics, whereas in the high temperature range, parabolic oxidation is followed by a breakaway transition to an increasing oxidation rate. The activation energy for parabolic oxidation from 937° - 991°C is 30 kcal/mole.

(ii) The break in the Arrhenius plot of the parabolic rate constants, between the temperatures 885°C and 937°C, is related to the $\alpha + \beta/\beta$ phase boundary of Zr-Nb phase diagram. In the range 650° - 885°C, the alloy is oxidized in the two phase $\alpha + \beta$ region whereas at and above 937°C, the alloy is fully in the β region.

(iii) During parabolic behaviour in the high temperature range, the α-Zr, exhibiting a columnar morphology, is stabilized below the oxide scale by inward diffusing oxygen. In the region of breakaway oxidation,

the α layer breaks down and rapid oxidation of the β-Zr takes place.

(iv) In the high temperature range a multiphase oxide scale is formed. The inner oxide layer, adjacent to the alloy/oxide interface, consists of columnar grains of monoclinic zirconia with intercolumnar regions of niobium enriched zirconia. The outer layer and main bulk of the oxide scale consists of a multiphase oxide of columnar grains of monoclinic zirconia with intercolumnar regions of the mixed oxide, $6ZrO_2 \cdot Nb_2O_5$.

(v) A zone of internal oxidation of $\alpha + ZrO_2(Nb)$ is formed beneath the oxide scale. The zirconia precipitates containing niobium occurred at the boundaries of the oxygen stabilized α plates. They formed as stringers extending continuously into the external scale and they appeared to exert a pinning action of the protective scale to the metal substrate.

(vi) The fine columnar structure of the internal oxidation zone is a result of the nucleation and growth of secondary α plates in the α precipitate region ahead of the advancing internal oxidation front. This phenomenon is attributed to the slope of the $\beta/\alpha + \beta$ phase boundary of the ternary isotherm which indicates a decreasing oxygen solubility with increasing niobium content. This yields sufficient oxygen supersaturation of β-Zr, in the $\alpha + \beta$ region, to allow precipitation of secondary plates of α-Zr.

(vii) The morphological development of the layered structure during parabolic kinetics at high temperatures is consistent with the available phase diagram data. The sequence of the observed layers is defined by a composition path crossing consecutive regions of the ternary isotherm between two terminal points defining a diffusion couple.

APPENDIX

TABLE I

PARABOLIC OXIDATION RATE CONSTANTS

Oxidation Temp.(^{o}C)	Sample	Kp($gm^2 cm^{-4} min^{-1}$)
1000	sphere	12.5×10^{-7}
	"	14.0×10^{-7}
991	plates	13.6×10^{-7}
	"	15.3×10^{-7}
	"	13.8×10^{-7}
937	"	8.17×10^{-7}
	"	7.88×10^{-7}
	"	8.89×10^{-7}
885	"	11.1×10^{-7}
	"	13.6×10^{-7}
832	"	7.25×10^{-7}
	"	8.14×10^{-7}
800	"	3.11×10^{-7}
750	"	1.54×10^{-7}
700	"	0.78×10^{-7}
650	"	0.17×10^{-7}

TABLE II

X-RAY DIFFRACTOMETER DATA

SPECIMEN: Oxide formed at 991°C (powdered)
RADIATION: CuK_α FILTER: Ni λ: 1.542Å

Peak	2θ	Specimen d(Å)	Specimen I/I_o	Monoclinic Zirconia (ASTM) d(Å)	Monoclinic Zirconia (ASTM) I/I_o
1	17.33	5.108	4	5.036	6
2	24.00	3.708	15	3.690	18
3	24.42	3.641	13	3.630	14
4	28.12	3.170	100	3.157	100
5	30.10	2.970	11		
6	31.40	2.846	73	2.843	65
7	34.14	2.623	23	2.617	20
8	34.25	2.608	20	2.598	12
9	35.22	2.545	18	2.538	14
				2.488	4
10	38.50	2.336	7	2.328	6
11	39.33	2.288	1	2.285	2
				2.252	4
12	40.67	2.215	17	2.213	14
13	41.27	2.184	8	2.182	6
14	44.74	2.023	8	2.015	8
15	45.40	1.995	7	1.989	8
16	49.22	1.849	25	1.845	18
17	50.10	1.819	35	1.818	12
18	50.50	1.805	21	1.801	12
19	51.16	1.783	11	1.780	6
20	54.00	1.696	17	1.691	14
21	55.27	1.660	20	1.656	14
22	55.85	1.644	13	1.640	8
23	57.16	1.610	10	1.608	8
24	57.88	1.591	7	1.591	4
25	58.08	1.586	8	1.581	4
26	59.84	1.544	17	1.541	10
27	61.30	1.510	8	1.508	6
28	61.88	1.498	8	1.495	10
29	62.74	1.479	14	1.476	6
30	64.23	1.448	3	1.447	4
31	65.62	1.421	11	1.420	6
32	68.85	1.362	1	1.358	2
				1.348	2
33	71.13	1.324	6	1.321	6
34	72.18	1.307	3	1.309	2
				1.298	2
35	75.06	1.264	6	1.269	2
36	78.95	1.211	3	+ 34 peaks to 0.885	

TABLE III

X-RAY DIFFRACTOMETER DATA

SPECIMEN: Oxide at the metal/oxide interface at 991°C (scale intact)
RADIATION: CuK_α FILTER: Ni λ: 1.542 Å

Peak	2θ	Specimen d(Å)	Specimen I/I_o	Monoclinic Zirconia (ASTM) d(Å)	Monoclinic Zirconia (ASTM) I/I_o
				5.036	6
1	24.06	3.694	11	3.690	18
2	24.45	3.623	3	3.630	14
3	28.22	3.158	100	3.157	100
4	31.48	2.838	16	2.843	65
5	34.14	2.623	10	2.617	20
6	34.40	2.600	6	2.598	12
7	35.28	2.540	2	2.538	14
8	35.85	2.501	3	2.488	4
9	38.60	2.329	4	2.328	6
				2.285	2
				2.252	4
10	40.75	2.212	5	2.213	14
11	41.45	2.176	4	2.182	6
12	44.85	2.014	3	2.015	8
13	45.52	1.990	15	1.989	8
14	49.26	1.847	18	1.845	18
15	50.15	1.816	7	1.818	12
16	50.58	1.802	21	1.801	12
17	51.27	1.780	4	1.780	6
18	54.10	1.693	2	1.691	14
19	55.40	1.656	10	1.656	14
20	55.58	1.651	12	1.640	8
21	57.20	1.608	2	1.608	8
22	57.48	1.601	2	1.591	4
23	58.30	1.580	6	1.581	4
24	59.94	1.541	4	1.541	10
25	60.14	1.536	4	1.508	6
26	61.99	1.495	8	1.495	10
				1.476	6
27	64.32	1.446	5	1.447	4
28	65.64	1.420	3	1.420	6
				1.358	2
				1.348	2
29	71.20	1.322	7	1.321	6
				1.309	2
				1.298	2
30	75.30	1.260	3	1.269	2
				+ 34 peaks to 0.885	

TABLE IV

OXYGEN DISTRIBUTION AT VARIOUS TEMPERATURES

Temperature (^{o}C)	w/o O_2 (in oxide)	w/o O_2 (in alloy)
1000	64%	36%
885	88%	12%
800	93%	7%
750	94%	6%
700	95%	5%
650	97%	3%

ELECTRON MICRO-PROBE RESULTS

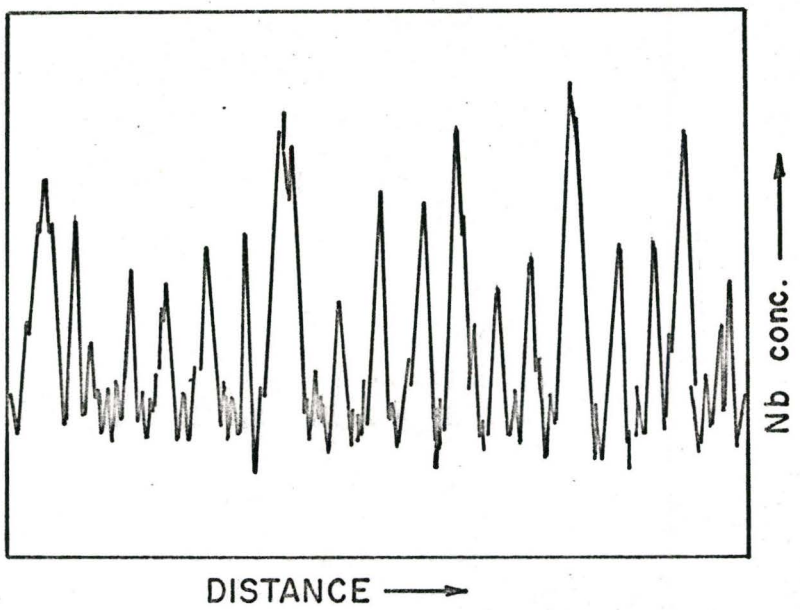

The above is the result of a transverse scan across the columnar structure of the $\alpha + \beta$ precipitate region showing the variation in niobium concentration. The large peaks were generated from the β-Zr areas between the columnar α-Zr plates, indicating niobium segregation in these regions. The lower limits of the scan were generated from the α-Zr plates indicating a lower solubility of Nb in α-Zr.

LIST OF REFERENCES

1. Hauffe, K.; "Oxidation of Metals", New York: Plenum Press, 1965.
2. Kofstad, P.; "High Temperature Oxidation of Metals", Waley and Sons, Inc., 1966.
3. Kubaschewski, O. and Hopkins, B. E.; "Oxidation of Metals and Alloys", London: Butterworth, 1962.
4. Cabrera, N. and Mott, N. F.; Repts. Prog. Phys., 12 (1949) 163.
5. Tammann,G.; Z. anorg. Chem., 111 (1920) 78.
6. Pilling, N. B. and Bedworth, R. E.; J. Inst. Met., 29 (1923) 529.
7. Wagner, C.; Z. Phys. Chem., B21 (1933) 25.
8. Wagner, C.; Atom Movements, A.S.M. (1951) 153.
9. Smeltzer, W. W. and Akram, H. K.; Can. Met. Quart., 1 (1962) 41.
10. Kubaschewski, O. and Hopkins, B. E.; "Oxidation of Metals and Alloys", London: Butterworth, 1962, Page 220.
11. Valens, G.; Rev. Métall., 45 (1948) 10.
12. Tylecote, R. F.; J. Inst. Met., 78 (1950) 259.
13. Hussey, R. J. and Smeltzer, W. W.; J. Electrochem. Soc., 111 (1964) 564.
14. Gulbransen, E. A. and Andrew, K. F.; J. Metals, 1 (1949) 515.
15. Smeltzer, W. W., Haerring, R. R. and Kirkaldy, J. S.; Acta Met., 9 (1961) 880.
16. Webb, W. W., Norton, J. T. and Wagner, C.; J. Electrochem. Soc., 103 (1956) 107.
17. Wallwork, G. R., Rosa, C. J., and Smeltzer, W. W.; Corrosion Sc., 5 (1965) 113.

18. Nomura, S. and Akutsu, C.; Electrochem. Tech., 4 (1966) 93.

19. Cox, B.; "Progress in Nuclear Energy, Series IV, Vol. 4, Technology, Engineering and Safety," Pergamon Press, (1961) 177.

20. Stringer, J.; Met. Rev., 11 (1966) 113.

21. Benard, J.; Met. Rev., 9 (1964) 473.

22. Wagner, C.; J. Electrochem. Soc., 103 (1956) 571.

23. Wagner, C.; J. Electrochem. Soc., 99 (1952) 369.

24. Wagner, C.; J. Electrochem. Soc., 103 (1956) 627.

25. Thomas, D. E.; J. Metals, 3 (1951) 926.

26. Rhines, R. N., Johnson, W. A., and Anderson, W. A.; Trans. AIME, 147 (1942) 205.

27. Moreau, J. and Benard, J.; Rev. Met., 59 (1962) 161.

28. Rapp, R. A.; Corrosion, 21 (1965) 382.

29. Belle, J. and Mallett, M. W.; J. Electrochem. Soc., 101 (1954) 339.

30. Charles, R. G. Barnartt, S. and Gulbransen, E. A.; Trans. AIME, 212 (1958) 101.

31. Gulbransen, E. A. and Andrew, K. F.; J. Metals, 9 (1957) 394.

32. Hillner, E.; Electrochem. Tech., 4 (1966) 132.

33. Porte, H. A., Schnizlein, J. G., Vogel, R. C. and Fischer, D. F.; J. Electrochem. Soc., 107 (1960) 507.

34. Pemsler, J. P.; Electrochem. Tech., 4 (1966) 128.

35. Wallwork, G. R., Smeltzer, W. W. and Rosa, C. J.; Acta Met., 12 (1964) 409.

36. Rosa, C. J. and Smeltzer, W. W.; Acta Met., 13 (1965) 55.

37. Pemsler, J. P.; J. Electrochem. Soc., 112 (1965) 477.

38. Rosa, C. J.; J. Less-Common Metals, 16 (1968) 173.

39. Hurlen, T.; J. Inst. Met., 89 (1960-1961) 273.

40. Sheasby, J. J., Wallwork, G. R. and Smeltzer, W. W.; J. Electrochem. Soc., 113 (1966) 1255.

41. Kofstad, P. and Espevik, S.; J. Electrochem. Soc., 112 (1965) 153.

42. Simms, C. T., Klopp, W. D. and Jaffee, R. I.; Trans. A.S.M., 51 (1959) 256.

43. Zmeskal, O. and Brey, M. L.; Trans. A.S.M., 53 (1961) 415.

44. Roth, R. S. and Coughanour, L. W.; J. Research, NBS, 54-55 (1955).

45. Rapp, R. A. and Goldberg, G. N.; Trans. AIME, 236 (1966) 1619.

46. Cowgill, M. G. and Smeltzer, W. W.; J. Electrochem. Soc., 114 (1967) 1089.

47. Cowgill, M. G., Wong, S. H. and Smeltzer, W. W.; J. Electrochem. Soc., 115 (1968) 927.

48. Guerlet, J. P and Lehr, P.; J. Nucl. Mater., 28 (1968) 165.

49. Elliott, R. P.; "Constitution of Binary Alloys, First Supplement", McGraw-Hill, New York (1965).

50. Winton, J. and Murgatroyd, R. A.; Electrochem. Tech., 4 (1966) 358.

51. Wyder, W. C. and Hoch, M.; Trans. AIME, 224 (1962) 373.

52. Clark, J. B. and Rhines, P. N.; Trans. A.S.M., 51 (1959) 199.

53. Kirkaldy, J. S. and Brown, L. C.; Can. Met. Quart., 2 (1963) 89.